Max-SINR ISI/ICI-Shaping Multicarrier Communication Over the Doubly Dispersive Channel

Sibasish Das and Philip Schniter

***Abstract*—For communication over doubly dispersive channels, we consider the design of multicarrier modulation (MCM) schemes based on time–frequency shifts of prototype pulses. We consider the case where the receiver knows the channel state and the transmitter knows the channel statistics (e.g., delay spread and Doppler spread) but not the channel state. Previous work has examined MCM pulses designed for suppression of inter-symbol/inter-carrier interference (ISI/ICI) subject to orthogonal or biorthogonal constraints. In doubly dispersive channels, however, complete suppression of ISI/ICI is impossible, and the ISI/ICI pattern generated by these (bi)orthogonal schemes can be difficult to equalize, especially when operating at high bandwidth efficiency. We propose a different approach to MCM pulse design, whereby a limited expanse of ISI/ICI is tolerated in modulation/demodulation and treated near-optimally by a downstream equalizer. Specifically, we propose MCM pulse designs that maximize a signal-to-interference-plus-noise ratio (SINR) which suppresses ISI/ICI outside a target pattern. In addition, we propose two low-complexity turbo equalizers, based on minimum mean-squared error and maximum likelihood criteria, respectively, that leverage the structure of the target ISI/ICI pattern. The resulting system exhibits an excellent combination of low complexity, low bit-error rate, and high spectral efficiency.**

***Index Terms*—Equalization, doubly dispersive channel, inter-carrier interference (ICI), inter-symbol interference (ISI), modulation, multicarrier, multipath, pulse-shape, time-varying channel, turbo-equalization, wireless communications.**

I. Introduction

MULTICARRIER modulation (MCM) is a popular transmission scheme in which the data stream is split into several substreams and transmitted, in parallel, on different subcarriers. We consider MCM over time-varying multipath propagation channels which spread the MCM signal simultaneously in both the time and frequency domains. This spreading induces both inter-symbol interference (ISI) and inter-carrier interference (ICI) which complicate data demodulation.

Among the most popular MCM schemes for communication over the doubly dispersive (DD) channel are those based on time–frequency shifts of prototype pulses, e.g., [1]–[6]. In the so-called QAM-MCM schemes, quadrature amplitude modulated (QAM) symbols $\{s_{k,l}\}$ are linearly modulated on pulses $\{a_{k,l}(t)\}$, where $a_{k,l}(t)$ is the kth time shift and lth frequency shift of prototype pulse $a_{0,0}(t)$. The received signal, noisy and dispersed, is then applied to a bank of "matched filters" $\{b_{k,l}(t)\}$ constructed by time–frequency shifts of prototype pulse $b_{0,0}(t)$. In orthogonal schemes, the pulses $a_{0,0}(t)$ and $b_{0,0}(t)$ are chosen so that $b_{k,l}(t) = a_{k,l}(t)$ and $\langle a_{k,l}(t), a_{m,n}(t)\rangle = \delta_{k-m}\delta_{l-n}$, while in biorthogonal schemes they are chosen so that $b_{k,l}(t) \neq a_{k,l}(t)$ and $\langle a_{k,l}(t), b_{m,n}(t)\rangle = \delta_{k-m}\delta_{l-n}$. Here, $\langle\cdot,\cdot\rangle$ denotes the inner product.

With *non*-dispersive channels, these (bi)orthogonal (BO) schemes guarantee zero ISI/ICI. For DD channels, however, ISI/ICI is impossible to avoid unless the pulses are designed with knowledge of the channel state. With such quickly varying channels, it is infeasible for the transmitter to track the channel's state, though feasible for it to track the channel's statistics (e.g., delay and Doppler spreads). In this case, it is possible to design MCM pulses which suppress ISI/ICI, e.g., by minimizing total ISI/ICI power. But there are two disadvantages with this approach. First, significant ISI/ICI suppression is possible only when the symbol rate is reduced to 50%–80% of the Nyquist rate [6]—a consequence of the Balian–Low theorem from Gabor theory [7]—and such a low "modulation efficiency" is generally undesirable. Second, the ISI/ICI that results from these pulses is usually spread across a multitude of subcarriers/symbols and, thus, is expensive to equalize.

In search of high modulation efficiency and simple yet high-performance equalization/decoding, we take a different approach to DD-channel QAM-MCM system design: rather that trying to suppress *all* ISI/ICI, we try to suppress only the ISI/ICI outside a *target pattern*. By careful selection of the target pattern, the dominant ISI/ICI within can be treated in a near-optimal manner by a simple detection algorithm. To shape the ISI/ICI response according to the target pattern, we design pulses which maximize a particular signal-to-interference-plus-noise ratio (SINR), leveraging an assumed knowledge of channel statistics (but not channel state). In particular, our SINR is defined so that "interference" measures out-of-target ISI/ICI power. Because we are interested in DD (rather than nondispersive) channels, we do not need to enforce the (bi)orthogonality constraint when designing our max-SINR pulses. Consequently, we are free to signal at the Nyquist rate. In summary, we propose a non-(bi)orthogonal (NBO) QAM-MCM scheme based on ISI/ICI *shaping* rather than ISI/ICI *suppression*. Though our approach could be extended to offset-QAM transmission [5] and/or nonrectangular time–frequency lattices [6], we do not do so here for reasons of space.

Manuscript received April 14, 2006; revised May 6, 2007. The associate editor coordinating the review of this paper and approving it for publication was Dr. Kostas Berberidis. This work was supported by Motorola Inc., by the National Science Foundation under Grants 0219892 and 0237037, and by the Office of Naval Research under Grant N00014-07-1-0209.

The authors are with the Department of Electrical and Computer Engineering, The Ohio State University, Columbus, OH 43210 USA (e-mail: dass@ece.osu.edu; schniter@ece.osu.edu).

Color versions of one or more of the figures in this paper are available online at http://ieeexplore.ieee.org.

Digital Object Identifier 10.1109/TSP.2007.901660

Through two novel equalization/decoding algorithms, we demonstrate that a well-designed ISI/ICI target pattern supports simple yet high-performance detection. Specifically, we assume bit-level convolutional coding and interleaving, and propose two novel soft-input soft-output (SISO) equalizers and combine them with a standard SISO decoder in a turbo-style configuration [8]. The first scheme, based on linear minimum mean-squared error (MMSE) equalization, builds on the work of Tüchler *et al.* [9]. The second scheme, based on maximum likelihood (ML) equalization, builds on the probabilistic data association (PDA) algorithm [10], [11]. The complexity and coded bit-error rate (BER) were numerically evaluated to demonstrate that the proposed QAM-MCM schemes compare well relative to other known schemes.

We now discuss our work in relation to previously proposed NBO-QAM-MCM schemes. Matheus and Kammeyer [12], [13] proposed a scheme based on Gaussian prototype pulses dilated to *suppress* ICI and/or ISI. In contrast, our pulses are not Gaussian-constrained and *tolerate* ISI/ICI within a target pattern. Hunziker and Dahlhaus [14] proposed a scheme using a Gaussian modulation pulse that minimized an out-of-target ISI/ICI metric, but they focused on time-dispersive, rather than doubly dispersive, channels. In previous work [15], we proposed a receiver for uncoded BPSK cyclic prefix (CP) orthogonal frequency division multiplexing (OFDM) over DD channels based on ISI-suppressing demodulation pulses and soft iterative ICI cancellation. In the current work, we consider *joint* design of modulation and demodulation pulses, and consequently treat both ISI and ICI in pulse design. In addition, we derive bit-level turbo-equalization algorithms based on the maximum *a posteriori* (MAP) criterion and perform a detailed numerical comparison with other schemes. Ma and Giannakis [16] proposed a linear modulation scheme with time- and frequency-domain guard intervals that excite the full diversity of the DD channel. Diversity maximization, however, comes at the cost of reduced spectral efficiency and high decoding complexity, even when suboptimal detection algorithms (e.g., [17]) are employed. We compare this maximum-diversity linear precoding (MDLP) scheme to various QAM-MCM schemes in the sequel.

The paper is structured as follows. Section II describes the system model, Section III derives max-SINR pulse designs, and Section IV details the turbo equalization algorithms. Section V investigates the complexity and performance of various QAM-MCM schemes and of MDLP, and Section VI concludes.

Notation: We use $(\cdot)^t$ to denote transpose, $(\cdot)^*$ conjugate, and $(\cdot)^H$ conjugate transpose. $\mathcal{C}(\boldsymbol{b})$ denotes the circulant matrix with first column $\boldsymbol{b}$, $\mathcal{D}(\boldsymbol{b})$ the diagonal matrix created from vector $\boldsymbol{b}$, $\mathbf{1}_K$ the vector of length K with each element equal to one, and $\boldsymbol{I}_K$ the $K \times K$ identity matrix. We use $[\boldsymbol{B}]_{m,n}$ to denote the element in the mth row and nth column of $\boldsymbol{B}$, where row/column indices begin with zero. Furthermore, $\|\cdot\|_F$ denotes the Frobenius norm, $\odot$ element-wise multiplication, $E\{\cdot\}$ expectation, $\boldsymbol{\Sigma}_{\boldsymbol{b},\boldsymbol{c}} := E\{\boldsymbol{b}\boldsymbol{c}^H\} - E\{\boldsymbol{b}\}E\{\boldsymbol{c}^H\}$ cross-covariance, and $\boldsymbol{\Sigma}_{\boldsymbol{b}} := E\{\boldsymbol{b}\boldsymbol{b}^H\} - E\{\boldsymbol{b}\}E\{\boldsymbol{b}^H\}$ auto-covariance. Finally, $\delta(\cdot)$ denotes the Kronecker delta, and $\mathbb{Z}$ the set of integers.

II. System Model

This section derives a discrete baseband model for the N-subcarrier coded QAM-MCM scheme assumed throughout the paper. At each multicarrier (MC) symbol index $i \in \mathbb{Z}$, a vector of coded interleaved bits $\boldsymbol{c}^{(i)} := \left[\boldsymbol{c}_0^{(i)t}, \boldsymbol{c}_1^{(i)t}, \ldots, \boldsymbol{c}_{N-1}^{(i)t}\right]^t$, where $\boldsymbol{c}_k^{(i)} := \left[c_{k,0}^{(i)}, c_{k,1}^{(i)}, \ldots, c_{k,M-1}^{(i)}\right]^t \in \{0,1\}^M$, is mapped to a vector of QAM symbols, $\boldsymbol{s}^{(i)} := \left[s_0^{(i)}, s_1^{(i)}, \ldots, s_{N-1}^{(i)}\right]^t \in \mathbb{S}^N$ by the symbol mapping $\psi : \{0,1\}^M \to \mathbb{S}$. Here, $\mathbb{S}$ is a Gray-mapped unit-energy QAM constellation of size $|\mathbb{S}| = 2^M$. These coded QAM symbols are used to modulate pulsed subcarriers as follows:

$$t_n = \sum_{i=-\infty}^{\infty} a_{n-iN_s} \frac{1}{\sqrt{N}} \sum_{k=0}^{N-1} s_k^{(i)} e^{j(2\pi/N)(n-iN_s-N_o)k}. \quad (1)$$

In (1), $\{a_n\}$ is the discrete-time modulation pulse, N_s is the MC-symbol interval (i.e., the number of channel uses between the start of one MC-symbol and the start of the next), and $N_o \in \{0, \ldots, N-1\}$ is the offset between the subcarrier-phase origin and the pulse origin. Note that this system transmits at an average rate of N/N_s QAM-symbols per channel use. We define the effective "guard length" $N_g := N_s - N$, such that $N_g = 0$ leads to an average rate of one QAM-symbol per channel use, i.e., Nyquist-rate signaling.

The multipath channel is described by its time-variant impulse response $h(n,l)$, defined as the time-n response to an impulse applied at time $n-l$. We assume a causal impulse response of length N_h. The signal observed by the receiver is

$$r_n = \sum_{l=0}^{N_h-1} h(n,l) t_{n-l} + \nu_n \quad (2)$$

where ν_n denotes circular white Gaussian noise (CWGN) with variance σ^2. Employing the wide-sense stationary uncorrelated scattering (WSSUS) assumption [18], we have $E\{h(n,l)h^*(n-q, l-m)\} = \rho_q \sigma_l^2 \delta(m)$, where ρ_q denotes the normalized temporal correlation (i.e., $\rho_0 = 1$) and σ_l^2 denotes the variance of the lth lag. Defining $r_n^{(i)} := r_{iN_s+n}$, $\nu_n^{(i)} := \nu_{iN_s+n}$, and $h^{(i)}(n,l) := h(iN_s+n, l)$, it follows that

$$r_n^{(i)} = \sum_{l=0}^{N_h-1} h^{(i)}(n,l) \sum_{\ell=-\infty}^{\infty} a_{\ell N_s+n-l} \frac{1}{\sqrt{N}} \times \sum_{k=0}^{N-1} s_k^{(i-\ell)} e^{j(2\pi/N)(n-l+\ell N_s-N_o)k} + \nu_n^{(i)}. \quad (3)$$

To estimate the MC-symbol $\boldsymbol{s}^{(i)}$, the receiver employs the pulse sequence $\{b_n\}$ as follows:

$$x_d^{(i)} = \frac{1}{\sqrt{N}} \sum_n r_n^{(i)} b_n e^{-j(2\pi/N)d(n-N_o)}. \quad (4)$$

As before, N_o delays the carrier origin relative to the pulse origin. Note that this system reduces to CP-OFDM [19] when

$N_o = N_g$, $\{a_n = 1\}_{n=0}^{N_s-1}$, and $\{b_n = 1\}_{n=N_o}^{N_s-1}$ (else $a_n = b_n = 0$). Plugging (3) into (4), we find

$$x_d^{(i)} = \sum_{\ell} \sum_{k=0}^{N-1} H^{(i,\ell)}(d-k,k) s_k^{(i-\ell)} + w_d^{(i)} \tag{5}$$

where

$$w_d^{(i)} := \frac{1}{\sqrt{N}} \sum_n b_n \nu_n^{(i)} e^{-j(2\pi/N)d(n-N_o)} \tag{6}$$

$$H^{(i,\ell)}(d,k) := \frac{1}{N} \sum_n \sum_{l=0}^{N_h-1} h^{(i)}(n,l) b_n a_{\ell N_s+n-l} \times e^{-j(2\pi/N)d(n-N_o)} e^{-j(2\pi/N)k(l-\ell N_s)}. \tag{7}$$

Equation (5) indicates that $H^{(i,\ell)}(d,k)$ can be interpreted as the response, at MC-symbol i and subcarrier $k+d$, to a frequency-domain impulse applied at MC-symbol $i-\ell$ and subcarrier k. With finite-duration causal pulses $\{a_n\}$ and $\{b_n\}$ of length N_a and N_b, respectively, only a finite number of terms in the set $\{H^{(i,\ell)}(d,k), \ell \in \mathbb{Z}\}$ will be nonzero. In this case, it can be shown that $H^{(i,\ell)}(d,k)$ will be nonzero for $\ell \in \{-L_{\mathsf{pre}}, \ldots, L_{\mathsf{pst}}\}$ where $L_{\mathsf{pre}} = \lfloor (N_b-1)/N_s \rfloor$ and $L_{\mathsf{pst}} = \lfloor (N_a+N_h-2)/N_s \rfloor$.

With $\boldsymbol{x}^{(i)} := \left[x_0^{(i)}, \ldots, x_{N-1}^{(i)}\right]^t$, $\boldsymbol{w}^{(i)} := \left[w_0^{(i)}, \ldots, w_{N-1}^{(i)}\right]^t$, and $[\boldsymbol{H}^{(i,\ell)}]_{d,k} := H^{(i,\ell)}(d-k,k)$, (5) implies the linear time-varying (LTV) system

$$\boldsymbol{x}^{(i)} = \sum_{\ell=-L_{\mathsf{pre}}}^{L_{\mathsf{pst}}} \boldsymbol{H}^{(i,\ell)} \boldsymbol{s}^{(i-\ell)} + \boldsymbol{w}^{(i)}. \tag{8}$$

For any i, nonzero $\{\boldsymbol{H}^{(i,\ell)}\}_{\ell \neq 0}$ causes ISI and nonzero off-diagonal elements in $\boldsymbol{H}^{(i,0)}$ cause ICI. In the sequel, we refer to $\{\boldsymbol{H}^{(i,\ell)}\}_{\ell<0}$ as pre-cursor ISI and $\{\boldsymbol{H}^{(i,\ell)}\}_{\ell>0}$ as post-cursor ISI.

III. Pulse Design

The pulses $\{a_n\}$ and $\{b_n\}$ affect the ISI/ICI patterns of the system (8). When only the channel statistics are known at the transmitter, it is possible to shape—though not suppress—the ISI/ICI caused by a DD channel. As described in Section I, we are interested in shaping the ISI/ICI into a form that allows simple yet high-performance equalization. Between shaped responses which contain only ICI, only ISI, or joint ISI/ICI, we find ICI-only responses to be the most convenient: ICI-only responses can be optimally mitigated in a block-by-block manner, whereas ISI-only responses would require per-subcarrier sequence-detection and joint-ISI/ICI responses would require two-dimensional sequence-detection (e.g., [13]). For this reason, we focus on pulse designs that aim to suppress ISI completely and yield a convenient ICI support region.

The low-pass nature of typical Doppler spectra motivates us to shape the ICI so that each subcarrier experiences interference from only $\pm D$ neighboring subcarriers. In other words, we are interested in LTV system responses with $\boldsymbol{H}^{(i,0)}$ having the quasi-banded support region illustrated in Fig. 1 and with zero-valued $\{\boldsymbol{H}^{(i,\ell)}\}_{\ell \neq 0}$, i.e., no ISI. Henceforth, we refer to this desired ISI/ICI support region as the "target." Generally speaking, larger values of D will allow better suppression of out-of-target ISI/ICI, and, hence, better equalization performance, at the expense of higher equalization complexity. A rough design rule for D can be obtained as follows. Since the subcarrier spacing in our system is $(T_c N)^{-1}$ Hz, where T_c denotes the sampling (or "chip") interval of the discrete-time system (1), a Doppler spread of $\pm f_{\mathsf{d}}$ Hz corresponds to a Doppler spread of $\pm f_{\mathsf{d}} T_c N$ subcarriers. For this reason, we set the target-ICI radius at $D = \lceil f_{\mathsf{d}} T_c N + \alpha \rceil$, where both performance and complexity increase with design parameter α. In Section V, we study the choice of D experimentally, and find $\alpha = 1$ to yield a good performance/complexity tradeoff.

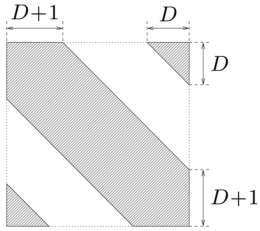

Fig. 1. Desired support region of cursor coefficient matrix $\boldsymbol{H}^{(i,0)}$.

A. An SINR Criterion

We design pulses according to an $\mathrm{SINR} := \mathcal{E}_{\mathsf{s}}/\mathcal{E}_{\mathsf{ni}}$ criterion, where signal energy $\mathcal{E}_{\mathsf{s}}$ and noise-plus-interference energy $\mathcal{E}_{\mathsf{ni}}$ are defined relative to the target ISI/ICI support region. If we define $\mathcal{E}_{\mathsf{s},d}$ to be the energy contributed to received-subcarrier $x_d^{(i)}$ by transmitted-subcarrier $s_d^{(i)}$, and if we define $\mathcal{E}_{\mathsf{ni},d}$ to be the energy contributed to received-subcarrier $x_d^{(i)}$ by additive noise $w_d^{(i)}$, pre- and post-cursor ISI $\left\{s_d^{(j)}\right\}_{j \neq i}$, and out-of-target ICI $\left\{s_k^{(i)}\right\}_{k=0}^{d-D-1} \cup \left\{s_k^{(i)}\right\}_{k=d+D+1}^{N-1}$, then $\mathcal{E}_{\mathsf{s}} = \sum_{d=0}^{N-1} \mathcal{E}_{\mathsf{s},d}$ and $\mathcal{E}_{\mathsf{ni}} = \sum_{d=0}^{N-1} \mathcal{E}_{\mathsf{ni},d}$ are defined by summing over subcarriers. When optimizing $\boldsymbol{a} := [a_0, \ldots, a_{N_a-1}]^t$, we impose the transmitter power constraint $\|\boldsymbol{a}\|^2 = N_s$.

Assuming uncorrelated unit-variance QAM-symbols in (5), we have

$$\mathcal{E}_{\mathsf{s}} = \sum_{d=0}^{N-1} E\left\{|H^{(i,0)}(0,d)|^2\right\}. \tag{9}$$

Using the WSSUS assumption with (7)

$$E\left\{|H^{(i,\ell)}(d,k)|^2\right\} = \frac{1}{N^2} \sum_{n,m=0}^{N_b-1} \rho_{n-m} b_n b_m^* \times e^{-j(2\pi/N)d(n-m)} \sum_{l=0}^{N_h-1} \sigma_l^2 a_{\ell N_s+n-l} a_{\ell N_s+m-l}^* \tag{10}$$

implying that

$$\mathcal{E}_{\mathsf{s}} = \frac{1}{N} \sum_{n=0}^{N_b-1} \sum_{m=0}^{N_b-1} b_n b_m^* \rho_{n-m} \sum_{l=0}^{N_h-1} \sigma_l^2 a_{n-l} a_{m-l}^*. \tag{11}$$

Equation (11) can be put in the quadratic forms (12) and (13)

$$\mathcal{E}_{\mathsf{s}} = \frac{1}{N} \boldsymbol{b}^H (\boldsymbol{R}_b \odot \boldsymbol{A}_{\mathsf{s}}) \boldsymbol{b} \tag{12}$$

$$= \frac{1}{N} \boldsymbol{a}^H (\boldsymbol{R}_a \odot \boldsymbol{B}_{\mathsf{s}}) \boldsymbol{a} \tag{13}$$

where $\boldsymbol{R}_b$ and $\boldsymbol{A}_{\mathsf{s}}$ are $N_b \times N_b$ matrices defined element-wise as $[\boldsymbol{R}_b]_{m,n} := \rho_{n-m}$ and $[\boldsymbol{A}_{\mathsf{s}}]_{m,n} := \sum_{l=0}^{N_h-1} \sigma_l^2 a_{n-l} a_{m-l}^*$, and where $\boldsymbol{R}_a$ and $\boldsymbol{B}_{\mathsf{s}}$ are $N_a \times N_a$ matrices defined element-wise as $[\boldsymbol{R}_a]_{p,q} := \rho_{q-p}$ and $[\boldsymbol{B}_{\mathsf{s}}]_{p,q} := \sum_{l=0}^{N_h-1} \sigma_l^2 b_{q+l} b_{p+l}^*$.

Assuming uncorrelated QAM-symbols and noise, (5) yields

$$\begin{aligned}\mathcal{E}_{\mathsf{ni},d} = E\left\{\left|w_d^{(i)}\right|^2\right\} &+ \sum_{\ell=-L_{\mathsf{pre}}}^{L_{\mathsf{pst}}} \sum_{k=0}^{N-1} E\{|H^{(i,\ell)}(d-k,k)|^2\} \\ &- \sum_{k=d-D}^{d+D} E\{|H^{(i,0)}(d-k,k)|^2\} \end{aligned} \tag{14}$$

where, from (6)

$$\begin{aligned} E\left\{\left|w_d^{(i)}\right|^2\right\} &= \frac{1}{N} \sum_{n,m=0}^{N_b-1} b_n b_m^* E\left\{\nu_n^{(i)} \nu_m^{(i)*}\right\} \\ &\quad \times e^{-j(2\pi/N)d(n-m)} \\ &= \frac{1}{N} \sum_{n=0}^{N_b-1} |b_n|^2 \sigma^2. \end{aligned} \tag{15}$$

The identities $\sum_{k=0}^{N-1}\sum_{d=0}^{N-1} e^{-j\frac{2\pi}{N}(d-k)(n-m)} = N^2\delta(\langle n-m\rangle_N)$ and $\sum_{q=-D}^{D} e^{-j\frac{2\pi}{N}q(n-m)} = \sin(\frac{\pi}{N}(2D+1)(n-m))/\sin(\frac{\pi}{N}(n-m))$ then imply (16)–(18), shown at the bottom of the page, where $\boldsymbol{b} := [b_0, \ldots, b_{N_b-1}]^t$. In (17), $\boldsymbol{R}_b$ and $\boldsymbol{A}_{\mathsf{s}}$ are as previously defined, and $\boldsymbol{C}_b$, $\boldsymbol{D}_b$, and $\boldsymbol{A}_{\mathsf{t}}$ are $N_b \times N_b$ matrices defined element-wise as $[\boldsymbol{C}_b]_{m,n} := \delta(\langle n-m\rangle_N)$, $[\boldsymbol{D}_b]_{m,n} := \frac{1}{N}\sin(\frac{\pi}{N}(2D+1)(n-m))/\sin(\frac{\pi}{N}(n-m))$, and $[\boldsymbol{A}_{\mathsf{t}}]_{m,n} := \sum_{\ell=-L_{\mathsf{pre}}}^{L_{\mathsf{pst}}}\sum_{l=0}^{N_h-1} \sigma_l^2 a_{\ell N_s+n-l} a_{\ell N_s+m-l}^*$. In (18), $\boldsymbol{R}_a$ and $\boldsymbol{B}_{\mathsf{s}}$ are as previously defined, and $\boldsymbol{C}_a$, $\boldsymbol{D}_a$, and $\boldsymbol{B}_{\mathsf{t}}$ are $N_a \times N_a$ matrices defined element-wise as $[\boldsymbol{D}_a]_{p,q} := \frac{1}{N}\sin(\frac{\pi}{N}(2D+1)(q-p))/\sin(\frac{\pi}{N}(q-p))$, $[\boldsymbol{B}_{\mathsf{t}}]_{p,q} := \sum_{\ell=-L_{\mathsf{pre}}}^{L_{\mathsf{pst}}}\sum_{l=0}^{N_h-1} \sigma_l^2 b_{q+l-\ell N_s} b_{p+l-\ell N_s}^*$, and $[\boldsymbol{C}_a]_{p,q} := \delta(\langle q-p\rangle_N)$. Note that we used $\|\boldsymbol{a}\|^2 = N_s$ to write (18). Since SINR $= \mathcal{E}_{\mathsf{s}}/\mathcal{E}_{\mathsf{ni}}$ is not a function of $\|\boldsymbol{b}\|$, we are free to impose $\|\boldsymbol{b}\|^2 = N_s$ in the sequel.

B. Max-SINR Pulse Designs

1) Jointly Optimized Pulses: To optimize SINR $= \mathcal{E}_{\mathsf{s}}/\mathcal{E}_{\mathsf{ni}}$ jointly with respect to $\boldsymbol{a}$ and $\boldsymbol{b}$ under the constraints $\|\boldsymbol{a}\|^2 = \|\boldsymbol{b}\|^2 = N_s$, we alternate the optimizations in (19) and (20), shown at the bottom of the page, where $\boldsymbol{v}_\star(\boldsymbol{M},\boldsymbol{N})$ denotes the principle generalized eigenvector of the matrix pair $(\boldsymbol{M},\boldsymbol{N})$. Recall that $\boldsymbol{A}_{\mathsf{s}}$ and $\boldsymbol{A}_{\mathsf{t}}$ are functions of $\boldsymbol{a}$ and that $\boldsymbol{B}_{\mathsf{s}}$ and $\boldsymbol{B}_{\mathsf{t}}$ are functions of $\boldsymbol{b}$. This optimization can be carried out in advance for particular channel statistics (e.g., Doppler/delay spreads). Examples of these jointly optimized max-SINR (JOMS) pulses are given in Fig. 8 for the system and channel parameters described in Section V.

$$\begin{aligned}\mathcal{E}_{\mathsf{ni}} = \sigma^2 &\sum_{n=0}^{N_b-1} |b_n|^2 \\ &+ \sum_{n=0}^{N_b-1}\sum_{m=0}^{N_b-1} b_n b_m^* \rho_{n-m} \delta(\langle n-m\rangle_N) \sum_{\ell=-L_{\mathsf{pre}}}^{L_{\mathsf{pst}}} \sum_{l=0}^{N_h-1} \sigma_l^2 a_{\ell N_s+n-l} a_{\ell N_s+m-l}^* \\ &- \sum_{n=0}^{N_b-1}\sum_{m=0}^{N_b-1} b_n b_m^* \rho_{n-m} \frac{\sin\left(\frac{\pi}{N}(2D+1)(n-m)\right)}{N\sin\left(\frac{\pi}{N}(n-m)\right)} \sum_{l=0}^{N_h-1} \sigma_l^2 a_{n-l} a_{m-l}^* \end{aligned} \tag{16}$$

$$= \boldsymbol{b}^H \left(\sigma^2 \boldsymbol{I}_{N_b} + \boldsymbol{R}_b \odot \boldsymbol{C}_b \odot \boldsymbol{A}_{\mathsf{t}} - \boldsymbol{R}_b \odot \boldsymbol{D}_b \odot \boldsymbol{A}_{\mathsf{s}}\right) \boldsymbol{b} \tag{17}$$

$$= \boldsymbol{a}^H \left(\|\boldsymbol{b}\|^2 \frac{\sigma^2}{N_s} + \boldsymbol{R}_a \odot \boldsymbol{C}_a \odot \boldsymbol{B}_{\mathsf{t}} - \boldsymbol{R}_a \odot \boldsymbol{D}_a \odot \boldsymbol{B}_{\mathsf{s}}\right) \boldsymbol{a} \tag{18}$$

$$\begin{aligned}\boldsymbol{b}_{\star|\boldsymbol{a}} &= \arg \max_{\boldsymbol{b}:\|\boldsymbol{b}\|^2=N_s} \frac{\boldsymbol{b}^H\left(\boldsymbol{R}_b \odot \boldsymbol{A}_{\mathsf{s}}\right)\boldsymbol{b}}{\boldsymbol{b}^H\left(\sigma^2\boldsymbol{I} + \boldsymbol{R}_b \odot \boldsymbol{C}_b \odot \boldsymbol{A}_{\mathsf{t}} - \boldsymbol{R}_b \odot \boldsymbol{D}_b \odot \boldsymbol{A}_{\mathsf{s}}\right)\boldsymbol{b}} \\ &= \boldsymbol{v}_\star\left(\boldsymbol{R}_b \odot \boldsymbol{A}_{\mathsf{s}},\ \sigma^2\boldsymbol{I} + \boldsymbol{R}_b \odot \boldsymbol{C}_b \odot \boldsymbol{A}_{\mathsf{t}} - \boldsymbol{R}_b \odot \boldsymbol{D}_b \odot \boldsymbol{A}_{\mathsf{s}}\right) \cdot \sqrt{N_s} \end{aligned} \tag{19}$$

$$\begin{aligned}\boldsymbol{a}_{\star|\boldsymbol{b}} &= \arg \max_{\boldsymbol{a}:\|\boldsymbol{a}\|^2=N_s} \frac{\boldsymbol{a}^H\left(\boldsymbol{R}_a \odot \boldsymbol{B}_{\mathsf{s}}\right)\boldsymbol{a}}{\boldsymbol{a}^H\left(\sigma^2\boldsymbol{I} + \boldsymbol{R}_a \odot \boldsymbol{C}_a \odot \boldsymbol{B}_{\mathsf{t}} - \boldsymbol{R}_a \odot \boldsymbol{D}_a \odot \boldsymbol{B}_{\mathsf{s}}\right)\boldsymbol{a}} \\ &= \boldsymbol{v}_\star\left(\boldsymbol{R}_a \odot \boldsymbol{B}_{\mathsf{s}},\ \sigma^2\boldsymbol{I} + \boldsymbol{R}_a \odot \boldsymbol{C}_a \odot \boldsymbol{B}_{\mathsf{t}} - \boldsymbol{R}_a \odot \boldsymbol{D}_a \odot \boldsymbol{B}_{\mathsf{s}}\right) \cdot \sqrt{N_s} \end{aligned} \tag{20}$$

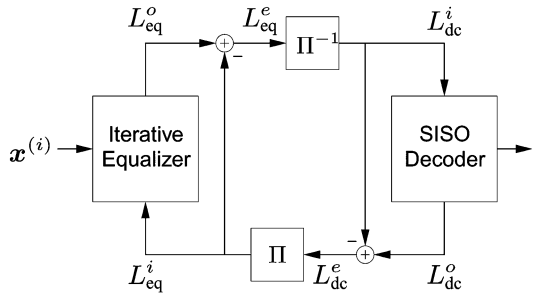

Fig. 2. Turbo receiver configuration.

2) Rectangularly Constrained Pulses: The JOMS demodulation pulses generally result in correlated noise samples $\left\{w_d^{(i)}\right\}$, which may pose difficulties for equalization/decoding algorithms. To ensure white noise samples, we could design transmitter-optimized max-SINR (TOMS) pulses using (20) in conjunction with the rectangular receiver pulse (21)

$$b_n = \begin{cases} 0, & 0 \le n < N_h - 1 \\ \sqrt{\frac{N_s}{N}}, & N_h \le n < N + N_h = N_b. \end{cases} \tag{21}$$

We could also design receiver-optimized max-SINR (ROMS) pulses using (19) in conjunction with a rectangular transmitter pulse. The latter scheme differs from traditional CP-OFDM in that ISI would be near-perfectly suppressed *without* a guard interval, and, thus, with higher modulation efficiency. TOMS and ROMS pulse examples appear in Fig. 8 for the parameters outlined in Section V. We note that other pulse constraints, e.g., max-SINR Gaussian pulses [20], might also be considered.

IV. Equalization

We consider the turbo equalization/decoding [8], [21] architecture illustrated in Fig. 2. The equalizer uses the observation $\boldsymbol{x}^{(i)}$ to update bit-reliability metrics referred to as L-values (LVs), the extrinsic components of which are de-interleaved and passed to the SISO decoder. The decoder then updates the LVs, the extrinsic components of which are interleaved and passed back to the equalizer. After initializing the LVs at zero, the equalizer and decoder iterate several times before final bit decisions are made. In Fig. 2, L_{eq} and L_{dc} denote the equalizer and decoder LVs, respectively, on which the superscripts i, e, and o denote input, extrinsic, and output versions, respectively. The equalizer block itself is iterative in that its LVs may be internally updated several times before being passed to the decoder. Note that the equalizer leverages the ISI/ICI structure but not the code structure (e.g., it assumes independent bits), while the decoder leverages the code structure but not the ISI/ICI structure (e.g., it assumes white noise).

A. Local Interference Model

The pulse designs in Section III aim to suppress ISI completely and suppress ICI outside a D-subcarrier radius. When pulse-shaping is successful, we reason that good "local" estimates of $s_k^{(i)}$ can be generated using $\boldsymbol{x}_k^{(i)} := \left[x_{k-D}^{(i)}, \ldots, x_{k+D}^{(i)}\right]^t$ in place of $\boldsymbol{x}^{(i)}$. With this in mind, we write

$$\boldsymbol{x}_k^{(i)} = \boldsymbol{H}_k^{(i)} \boldsymbol{s}_k^{(i)} + \boldsymbol{\varepsilon}_k^{(i)} \tag{22}$$

where $\boldsymbol{H}_k^{(i)} := [\boldsymbol{H}^{(i,0)}]_{k-D:k+D,k-2D:k+2D}$, $\boldsymbol{s}_k^{(i)} := \left[s_{k-2D}^{(i)}, \ldots, s_{k+2D}^{(i)}\right]^t$, and where $\boldsymbol{\varepsilon}_k^{(i)}$ contains the noise $\boldsymbol{w}_k^{(i)} := \left[w_{k-D}^{(i)}, \ldots, w_{k+D}^{(i)}\right]^t$ plus residual ISI/ICI. *For brevity, all indexing in this section will be assumed modulo-N.* As a consequence, the elements of $\boldsymbol{H}^{(i,0)}$ from the top-right and bottom-left shaded triangles in Fig. 1 will be included in $\left\{\boldsymbol{H}_k^{(i)}\right\}_{k=0}^{N-1}$. Numerical studies suggest that, for the pulse designs of Section III and over the SNR range of interest, $\boldsymbol{\varepsilon}_k^{(i)}$ is well modeled by zero-mean circular Gaussian noise with covariance $\boldsymbol{\Sigma}_{\boldsymbol{\varepsilon}_k} = \boldsymbol{\Sigma}_{\boldsymbol{w}_k}$.

B. Bit Reliability Metric

Our equalizer uses the observation $\boldsymbol{x}^{(i)}$ and channel $\boldsymbol{H}^{(i,0)}$ to update the ith MC-symbol's bit LVs, collected as $\{L^{(i)}(k,m)\}_{k=0,m=0}^{N-1,M-1}$, where

$$L^{(i)}(k,m) := \ln \frac{P(c_{k,m}^{(i)} = 0 | \boldsymbol{x}^{(i)})}{P(c_{k,m}^{(i)} = 1 | \boldsymbol{x}^{(i)})}. \tag{23}$$

Since all quantities pertain to the ith MC-symbol, we omit superscript indices w.l.o.g. Note that the sign of $L(k,m)$ is the uncoded MAP bit decision and the magnitude of $L(k,m)$ indicates the reliability of this decision. Using Bayes' rule and assuming independent bits (as a consequence of interleaving), $L(k,m)$ can be rewritten as the sum of a prior LV, $L_{\text{old}}(k,m)$, and an extrinsic LV, $\Delta L(k,m)$, as in (24), shown at the bottom of the page. In (24), $\mathcal{G}_{k_2,\alpha}^{k_1}$ denotes the set of all length-k_1 bit vectors in which the k_2th bit has been set to $\alpha \in \{0,1\}$. Since the decoupling of $\Delta L(k,m)$ and $L_{\text{old}}(k,m)$ is important, we will be careful to ensure that $L_{\text{old}}(k,m)$ is not used to calculate $\Delta L(k,m)$.

Since exact computation of $\Delta L(k,m)$ is generally infeasible, we propose two suboptimal algorithms, detailed in Sections IV-C and D, based on approximations of $\Delta L(k,m)$

$$L(k,m) = \underbrace{\ln \frac{\sum_{\boldsymbol{\gamma} \in \mathcal{G}_{kM+m,0}^{NM}} p(\boldsymbol{x}|\boldsymbol{c}=\boldsymbol{\gamma}) \prod_{(k',m') \neq (k,m)} P(c_{k',m'} = \gamma_{k'M+m'})}{\sum_{\boldsymbol{\gamma} \in \mathcal{G}_{kM+m,1}^{NM}} p(\boldsymbol{x}|\boldsymbol{c}=\boldsymbol{\gamma}) \prod_{(k',m') \neq (k,m)} P(c_{k',m'} = \gamma_{k'M+m'})}}_{\Delta L(k,m)} + \underbrace{\ln \frac{P(c_{k,m}=0)}{P(c_{k,m}=1)}}_{L_{\text{old}}(k,m)} \tag{24}$$

that use the local observation $\boldsymbol{x}_k$ in place of $\boldsymbol{x}$. Both make use of the QAM-symbol means and variances

$$\mu_k = \sum_{\beta\in\mathbb{S}} \beta P(s_k=\beta) \tag{25}$$

$$v_k = \sum_{\beta\in\mathbb{S}} |\beta|^2 P(s_k=\beta) - |\mu_k|^2. \tag{26}$$

Note that, since Gray-mapping is assumed, the real and imaginary components of each QAM-symbol are independent, and, thus, $v_{k,R} := \mathrm{var}(\mathrm{Re}\, s_k)$ and $v_{k,I} := \mathrm{var}(\mathrm{Im}\, s_k)$ can be written

$$v_{k,R} = \sum_{\beta\in\mathbb{S}} (\mathrm{Re}\,\beta)^2 P(s_k=\beta) - (\mathrm{Re}\,\mu_k)^2 \tag{27}$$

$$v_{k,I} = \sum_{\beta\in\mathbb{S}} (\mathrm{Im}\,\beta)^2 P(s_k=\beta) - (\mathrm{Im}\,\mu_k)^2. \tag{28}$$

C. Iterative ML Equalizer (IMLE)

This technique derives its name from the fact that $\Delta L(k,m)$ is the maximum likelihood (ML) decision statistic for bit $c_{k,m}$. Here, however, $\Delta L(k,m)$ is approximated to reduce computational complexity. The key idea is to first perform a soft interference cancellation (SIC) using the QAM-symbol means $\{\mu_k\}$, then to apply a Gaussian model to the residual interference-plus-noise. The resulting $\Delta L(k,m)$ approximation, denoted by $\Delta L_{\mathrm{IMLE}}(k,m)$, is much easier to compute. Specifically, the partial observation after SIC is written

$$\begin{aligned}\boldsymbol{y}_k &= \boldsymbol{x}_k - \boldsymbol{H}_k\boldsymbol{\mu}_k \\ &= \boldsymbol{h}_{k,0}s_k + \boldsymbol{q}_k\end{aligned} \tag{29}$$

where $\boldsymbol{h}_{k,j}$ denotes the $(j+2D)$th column of $\boldsymbol{H}_k$ and where

$$\boldsymbol{q}_k = \sum_{\substack{j=k-2D \\ j\neq k}}^{k+2D} \boldsymbol{h}_{k,j}(s_j-\mu_j) + \boldsymbol{\varepsilon}_k \tag{30}$$

$$\boldsymbol{\mu}_k := [\mu_{k-2D},\ldots,\mu_{k-1},0,\mu_{k+1},\ldots,\mu_{k+2D}]^t. \tag{31}$$

The residual interference $\boldsymbol{q}_k$ is modeled as zero-mean Gaussian, independent of s_k, with covariance $\boldsymbol{\Sigma}_{\boldsymbol{q}_k}$

$$\boldsymbol{\Sigma}_{\boldsymbol{q}_k} = \boldsymbol{H}_k\mathcal{D}(\boldsymbol{v}_k)\boldsymbol{H}_k^H + \boldsymbol{\Sigma}_{\boldsymbol{\varepsilon}_k}, \tag{32}$$

$$\boldsymbol{v}_k := [v_{k-2D},\ldots,v_{k-1},0,v_{k+1},\ldots,v_{k+2D}]^t. \tag{33}$$

Replacing $p(\boldsymbol{x}|\boldsymbol{c}=\boldsymbol{\gamma})$ in (24) with $p(\boldsymbol{y}_k|s_k=\psi(\boldsymbol{\gamma}))$, the extrinsic LV becomes as shown in (34) at the bottom of the page. For simplicity, the remainder of the development assumes QPSK; the extension to general QAM is straightforward but tedious. For QPSK, Appendix A shows (35), also shown at the bottom of the page, where $g_k := \boldsymbol{y}_k^H\boldsymbol{\Sigma}_{\boldsymbol{q}_k}^{-1}\boldsymbol{h}_{k,0}$. Note again that $L_{\mathrm{old}}(k,m)$ is not used when computing $\Delta L_{\mathrm{IMLE}}(k,m)$.

The IMLE algorithm proceeds as follows. Prior to the first iteration, $\{L_{\mathrm{old}}(k,m)\ \forall\ k,m\}$ are obtained from the output of a soft decoder, if available, or otherwise set to zero. These LVs are then used to initialize $\{\mu_k\}_{k=0}^{N-1}$ and $\{v_k\}_{k=0}^{N-1}$. We begin the first iteration by working on subcarrier index $k=0$. The means $\boldsymbol{\mu}_0$ and variances $\boldsymbol{v}_0$ are used to calculate $\boldsymbol{y}_0$ and $\boldsymbol{\Sigma}_{\boldsymbol{q}_0}$, which in turn are used to compute g_0. From g_0 and $\{L_{\mathrm{old}}(0,m)\}_{m=0}^{M-1}$, $\{\Delta L_{\mathrm{IMLE}}(0,m)\}_{m=0}^{M-1}$ are calculated and used to compute $\{L(0,m)\}_{m=0}^{M-1}$. Finally, $\{L(0,m)\}_{m=0}^{M-1}$ are used to update μ_0 and v_0. Moving on to $k=1$, the vectors $\boldsymbol{\mu}_1$ and $\boldsymbol{v}_1$ are used to calculate $\boldsymbol{y}_1$ and $\boldsymbol{\Sigma}_{\boldsymbol{q}_1}$, and later g_1. This allows the computation of $\{\Delta L_{\mathrm{IMLE}}(1,m)\}_{m=0}^{M-1}$, the computation of $\{L(1,m)\}_{m=0}^{M-1}$, and the update of μ_1 and v_1. The $k=2$ case is tackled next, then $k=3$, and so on, until $k=N-1$. Finally, $\{L(k,m)\ \forall\ k,m\}$ are copied to $\{L_{\mathrm{old}}(k,m)\ \forall k,m\}$. This concludes the first iteration. The next (e.g., second) iteration begins again at subcarrier index $k=0$ and proceeds through $k=N-1$. The algorithm terminates after a specified number of iterations.

Table I summarizes the steps in one IMLE iteration. The mean, variance, and LV updates are derived in Appendix B. The computational complexity for IMLE is dominated by the inversion of the $(2D+1)\times(2D+1)$ matrix $\boldsymbol{\Sigma}_{q_k}$, yielding a per-iteration complexity order of $\mathcal{O}(ND^3)$. Because $\boldsymbol{\Sigma}_{q_k}$ and $\boldsymbol{\Sigma}_{q_{k-1}}$ share many elements, it is possible to update $\boldsymbol{\Sigma}_{q_k}^{-1}$ recursively (e.g., [22]) for complexity order of $\mathcal{O}(ND^2)$, though studies have shown that this is only advantageous for very large D (e.g., [23]).

Like [11], IMLE avoids the zero-forcing transformation in the original PDA scheme [10] and exploits structure in the channel matrix to reduce equalizer complexity. However, while IMLE works on the *bit* level, [11] works on the *symbol* level; it up-

$$\Delta L_{\mathrm{IMLE}}(k,m) = \ln \frac{\sum_{\boldsymbol{\gamma}\in\mathcal{G}_{m,0}^M} p\left(\boldsymbol{y}_k|s_k=\psi(\boldsymbol{\gamma})\right)\prod_{m'\neq m} P(c_{k,m'}=\gamma_{m'})}{\sum_{\boldsymbol{\gamma}\in\mathcal{G}_{m,1}^M} p\left(\boldsymbol{y}_k|s_k=\psi(\boldsymbol{\gamma})\right)\prod_{m'\neq m} P(c_{k,m'}=\gamma_{m'})} \tag{34}$$

$$\Delta L_{\mathrm{IMLE}}(k,m) = \ln \frac{\sum_{\boldsymbol{\gamma}\in\mathcal{G}_{m,0}^M} \exp\left[\mathrm{Re}\left(\psi(\boldsymbol{\gamma})g_k\right) + \frac{1}{2}\sum_{m'\neq m}(-1)^{\gamma_{m'}}L_{\mathrm{old}}(k,m')\right]}{\sum_{\boldsymbol{\gamma}\in\mathcal{G}_{m,1}^M} \exp\left[\mathrm{Re}\left(\psi(\boldsymbol{\gamma})g_k\right) + \frac{1}{2}\sum_{m'\neq m}(-1)^{\gamma_{m'}}L_{\mathrm{old}}(k,m')\right]} \tag{35}$$

TABLE I
STEPS IN ONE ITERATION OF IMLE-QPSK

```
for k = 0 : N − 1
  Σ_{q_k}^{-1} = (H_k D(v_k) H_k^H + Σ_{ε_k})^{-1}
  y_k = x_k − H_k μ_k
  g_k = y_k^H Σ_{q_k}^{-1} h_{k,0}
  L(k,0) = L_old(k,0) + √2 Re g_k
  L(k,1) = L_old(k,1) − √2 Im g_k
  μ_k = (1/√2) tanh(L(k,0)/2) + (j/√2) tanh(L(k,1)/2)
  v_k = 1 − |μ_k|^2
  L_old(k,0) = L(k,0),   L_old(k,1) = L(k,1)
end
```

dates soft *symbol* estimates from which bit values are later inferred using hard decisions. Also, [11] works in the time domain [i.e., (3)], while our scheme operates in the frequency domain [i.e., (5)]. While the time domain scheme requires $N_h \times N_h$ matrix inverses, the frequency domain scheme requires only $(2D+1) \times (2D+1)$ matrix inverses, which is significantly cheaper since, typically, $(2D+1) \ll N_h$.

D. Iterative MMSE Equalizer (IMSE)

Whereas in IMLE we performed SIC before computing extrinsic LVs, here we perform linear MMSE estimation before computing extrinsic LVs. The linear MMSE estimate of s_k using the partial observation $\boldsymbol{x}_k$ is [24]

$$\hat{s}_k\big|_{\text{MMSE}} = \mu_k + \boldsymbol{h}_{k,0}^H \left(\boldsymbol{\Sigma}_{\boldsymbol{\varepsilon}_k} + \boldsymbol{H}_k \boldsymbol{\Sigma}_{\boldsymbol{s}_k} \boldsymbol{H}_k^H\right)^{-1} (\boldsymbol{x}_k - E\{\boldsymbol{x}_k\}) \tag{36}$$

where the bit independence assumption implies that the covariance matrix $\boldsymbol{\Sigma}_{\boldsymbol{s}_k}$ is diagonal. However, to make $\Delta L(k,m)$ invariant to $L_{\text{old}}(k,m)$, we set $\mu_k = 0$ and $v_k = 1$ when estimating s_k, resulting in the "extrinsic" estimate

$$\hat{s}_k = \underbrace{\boldsymbol{h}_{k,0}^H \left(\boldsymbol{\Sigma}_{\boldsymbol{\varepsilon}_k} + \boldsymbol{H}_k \mathcal{D}(\boldsymbol{v}_k) \boldsymbol{H}_k^H + \boldsymbol{h}_{k,0} \boldsymbol{h}_{k,0}^H\right)^{-1}}_{\boldsymbol{f}_k^H} (\boldsymbol{x}_k - \boldsymbol{H}_k \boldsymbol{\mu}_k) \tag{37}$$

for $\boldsymbol{\mu}_k$ and $\boldsymbol{v}_k$ defined in (31) and (33), respectively. Finally, we assume that the estimation error, $\hat{s}_k - s_k$, is complex Gaussian with uncorrelated real and imaginary components. Equivalently, $\hat{s}_k$ is conditionally Gaussian with the means and variances

$$\bar{s}_{k,\boldsymbol{\gamma}} := E\{\hat{s}_k | s_k = \psi(\boldsymbol{\gamma})\} \tag{38}$$

$$\sigma_{k,R}^2 := E\left\{\text{Re}^2(\hat{s}_k - \bar{s}_{k,\boldsymbol{\gamma}}) | s_k = \psi(\boldsymbol{\gamma})\right\} \tag{39}$$

$$\sigma_{k,I}^2 := E\left\{\text{Im}^2(\hat{s}_k - \bar{s}_{k,\boldsymbol{\gamma}}) | s_k = \psi(\boldsymbol{\gamma})\right\}. \tag{40}$$

The quantities $\bar{s}_{k,\boldsymbol{\gamma}}$, $\sigma_{k,R}^2$, and $\sigma_{k,I}^2$ can be computed from $\boldsymbol{\mu}_k$ and $\boldsymbol{v}_k$ as shown in (41)–(45) at the bottom of the page (see Appendix C). Note that the conditional variances are not actually dependent on $\boldsymbol{\gamma}$. Replacing $p(\boldsymbol{x}|\boldsymbol{c} = \boldsymbol{\gamma})$ in (24) with $p(\hat{s}_k | s_k = \psi(\boldsymbol{\gamma}))$ and invoking our various assumptions, $\Delta L_{\text{IMSE}}(k,m)$ becomes (46) and (47), also shown at the bottom of the page (see Appendix D).

The IMSE algorithm cycles through the k and m indices in the same manner as IMLE. Table II summarizes the steps in one iteration of IMSE for QPSK. The mean, variance, and LV updates are derived in Appendix B. As in IMLE, the inverse matrix can be computed recursively.

$$\bar{s}_{k,\boldsymbol{\gamma}} = \psi(\boldsymbol{\gamma}) \boldsymbol{f}_k^H \boldsymbol{h}_{k,0} \tag{41}$$

$$\sigma_{k,R}^2 = \frac{1}{4} \begin{bmatrix} \boldsymbol{f}_k \\ \boldsymbol{f}_k^* \end{bmatrix}^H \begin{bmatrix} \boldsymbol{H}_k \mathcal{D}(\boldsymbol{v}_k) \boldsymbol{H}_k^H + \boldsymbol{\Sigma}_{\boldsymbol{\varepsilon}_k} & \boldsymbol{H}_k \mathcal{D}(\boldsymbol{v}_{k,R} - \boldsymbol{v}_{k,I}) \boldsymbol{H}_k^t \\ \boldsymbol{H}_k^* \mathcal{D}(\boldsymbol{v}_{k,R} - \boldsymbol{v}_{k,I}) \boldsymbol{H}_k^H & \boldsymbol{H}_k^* \mathcal{D}(\boldsymbol{v}_k) \boldsymbol{H}_k^t + \boldsymbol{\Sigma}_{\boldsymbol{\varepsilon}_k}^* \end{bmatrix} \begin{bmatrix} \boldsymbol{f}_k \\ \boldsymbol{f}_k^* \end{bmatrix} \tag{42}$$

$$\sigma_{k,I}^2 = \frac{1}{4} \begin{bmatrix} \boldsymbol{f}_k \\ -\boldsymbol{f}_k^* \end{bmatrix}^H \begin{bmatrix} \boldsymbol{H}_k \mathcal{D}(\boldsymbol{v}_k) \boldsymbol{H}_k^H + \boldsymbol{\Sigma}_{\boldsymbol{\varepsilon}_k} & \boldsymbol{H}_k \mathcal{D}(\boldsymbol{v}_{k,R} - \boldsymbol{v}_{k,I}) \boldsymbol{H}_k^t \\ \boldsymbol{H}_k^* \mathcal{D}(\boldsymbol{v}_{k,R} - \boldsymbol{v}_{k,I}) \boldsymbol{H}_k^H & \boldsymbol{H}_k^* \mathcal{D}(\boldsymbol{v}_k) \boldsymbol{H}_k^t + \boldsymbol{\Sigma}_{\boldsymbol{\varepsilon}_k}^* \end{bmatrix} \begin{bmatrix} \boldsymbol{f}_k \\ -\boldsymbol{f}_k^* \end{bmatrix} \tag{43}$$

$$\boldsymbol{v}_{k,R} = [v_{k-2D,R}, \ldots, v_{k-1,R}, 0, v_{k+1,R}, \ldots, v_{k+2D,R}]^t \tag{44}$$

$$\boldsymbol{v}_{k,I} = [v_{k-2D,I}, \ldots, v_{k-1,I}, 0, v_{k+1,I}, \ldots, v_{k+2D,I}]^t. \tag{45}$$

$$\Delta L_{\text{IMSE}}(k,m) = \ln \frac{\sum_{\boldsymbol{\gamma} \in \mathcal{G}_{m,0}^M} p(\hat{s}_k | s_k = \psi(\boldsymbol{\gamma})) \prod_{m' \neq m} P(c_{k,m'} = \gamma_{m'})}{\sum_{\boldsymbol{\gamma} \in \mathcal{G}_{m,1}^M} p(\hat{s}_k | s_k = \psi(\boldsymbol{\gamma})) \prod_{m' \neq m} P(c_{k,m'} = \gamma_{m'})} \tag{46}$$

$$= \ln \frac{\sum_{\boldsymbol{\gamma} \in \mathcal{G}_{m,0}^M} \exp\left[-\frac{\text{Re}^2(\hat{s}_k - \bar{s}_{k,\boldsymbol{\gamma}})}{2\sigma_{k,R}^2} - \frac{\text{Im}^2(\hat{s}_k - \bar{s}_{k,\boldsymbol{\gamma}})}{2\sigma_{k,I}^2} + \frac{1}{2} \sum_{m' \neq m} (-1)^{\gamma_{m'}} L_{\text{old}}(k,m')\right]}{\sum_{\boldsymbol{\gamma} \in \mathcal{G}_{m,1}^M} \exp\left[-\frac{\text{Re}^2(\hat{s}_k - \bar{s}_{k,\boldsymbol{\gamma}})}{2\sigma_{k,R}^2} - \frac{\text{Im}^2(\hat{s}_k - \bar{s}_{k,\boldsymbol{\gamma}})}{2\sigma_{k,I}^2} + \frac{1}{2} \sum_{m' \neq m} (-1)^{\gamma_{m'}} L_{\text{old}}(k,m')\right]} \tag{47}$$

TABLE II
STEPS IN ONE ITERATION OF IMSE-QPSK

for $k = 0 : N-1$,

$\boldsymbol{f}_k = \left(\boldsymbol{\Sigma}_{\boldsymbol{\epsilon}_k} + \boldsymbol{H}_k \mathcal{D}(\boldsymbol{v}_k)\boldsymbol{H}_k^H + \boldsymbol{h}_{k,0}\boldsymbol{h}_{k,0}^H\right)^{-1}\boldsymbol{h}_{k,0}$

$\hat{s}_k = \boldsymbol{f}_k^H\left(\boldsymbol{x}_k - \boldsymbol{H}_k\boldsymbol{\mu}_k\right)$

compute $\sigma_{k,R}^2$ and $\sigma_{k,I}^2$ from (42)-(43)

$L(k,0) = L_{\text{old}}(k,0) + \sqrt{2}\sigma_{k,R}^{-2}\,\text{Re}(\hat{s}_k)\boldsymbol{f}_k^H\boldsymbol{h}_{k,0}$

$L(k,1) = L_{\text{old}}(k,1) + \sqrt{2}\sigma_{k,I}^{-2}\,\text{Im}(\hat{s}_k)\boldsymbol{f}_k^H\boldsymbol{h}_{k,0}$

$\mu_k = \frac{1}{\sqrt{2}}\tanh\left(\frac{L(k,0)}{2}\right) + \frac{j}{\sqrt{2}}\tanh\left(\frac{L(k,1)}{2}\right)$

$v_{k,R} = \frac{1}{2} - (\text{Re}\,\mu_k)^2,\ v_{k,I} = \frac{1}{2} - (\text{Im}\,\mu_k)^2$

$L_{\text{old}}(k,0) = L(k,0),\quad L_{\text{old}}(k,1) = L(k,1)$

end

Like [9] and [15], IMSE is an iterative MMSE estimation algorithm. In both [9] and [15], however, the estimation error is modeled as complex *circular* Gaussian. Numerical studies conducted by the authors (but not reported here) have shown that IMSE's provision for $\sigma_{k,I}^2 \neq \sigma_{k,R}^2$ is essential when complex alphabets are used; the assumption $\sigma_{k,I}^2 = \sigma_{k,R}^2$ leads to significant performance loss. Also, [9] updates the symbol means and variances once per block (i.e., after updating $\{\Delta L(k,m), \forall m\}_{k=0}^{N-1}$), whereas IMSE updates the symbol means and variances at every k. Numerical studies have shown that symbol-rate updating leads to significant performance gains. Finally, [9] uses the full observation vector $\boldsymbol{x}$, requiring an $N \times N$ matrix inversion, whereas IMSE use the partial observation $\boldsymbol{x}_k$, requiring only $(2D+1) \times (2D+1)$ matrix inversion. Since $D \ll N$, this leads to significant computational savings.

V. NUMERICAL RESULTS

Here, we examine the BER performance of several coded QAM-MCM schemes over a WSSUS Rayleigh-fading channel [25]. This channel is defined by the statistical properties $E\{h(n,l)h^*(n-q,l-m)\} = \rho_q\sigma_l^2\delta(m)$, where $\rho_q = J_0(2\pi f_{\text{d}}T_c q)$. Here, $J_0(\cdot)$ denotes the zeroth-order Bessel function of the first kind, f_{d} denotes the single-sided Doppler spread—defined as the largest frequency shift that the transmitted signal experiences as a result of channel time-variation, and T_c denotes the sampling (or "chip") interval of the discrete-time system (1). We focus on normalized Doppler spread $f_{\text{d}}T_c = 0.003$, delay spread $N_h = 16$, and uniform delay-power profile (i.e., $\sigma_l^2 = N_h^{-1}\ \forall\ l$). These channel parameters correspond to, for example, an underwater acoustic system with bandwidth 4 kHz, delay spread 4 ms, and Doppler spread 12 Hz, or a mobile RF system with bandwidth 3 MHz, carrier frequency $f_c = 20$ GHz, delay spread $T_h = 5.4\ \mu$s, and mobile speed 160 km/hr in triple-Doppler conditions.[1] While our delay/Doppler spread parameters would be somewhat extreme in the mobile RF setting, they would not be unusual in the shallow-water acoustic communication setting [27].

A. Max-SINR QAM-MCM Performance

For the proposed max-SINR QAM-MCM schemes, information bits were coded using the 0.97dB-gain rate-1/2 convolutional code from [28, Table 11.c], block interleaved, Gray-mapped to QPSK symbols, and assigned to one of $N = 64$ subcarriers in a MC-symbol. The coding and interleaving[2] were performed on blocks of $N_i = 40$ MC-symbols.[3] We employed the MC-symbol interval $N_s = N$ (yielding an efficiency of $\eta = 1$ QPSK-symbols/s/Hz and, consequently, a rate of 1 information-bits/s/Hz). An ICI radius of $D = \lceil f_{\text{d}}T_c N + \alpha \rceil$ was assumed, where (as described below) $\alpha = 1$ was found to give a good balance between performance and complexity. For $f_{\text{d}}T_c = 0.003$, this rule yields $D = 2$. The pulse lengths were chosen to be large enough so that further length increases did not lead to visible changes in the max-SINR pulse shapes. Towards this aim, the rules $N_a = 1.5N_s$ and $N_b = N_a + N_h/2$ seemed to suffice for a wide range of N_s and N_h. A SISO BCJR decoder [29] was employed with one equalizer iteration per decoding iteration. Each BER data point represents the average of 4000 MC-symbols.

Fig. 3 shows BER versus SNR for several turbo-equalized max-SINR QAM-MCM systems relative to several bounds and reference traces. The MLk and MSk traces refer to IMLE and IMSE equalization, respectively, after k turbo iterations. In Fig. 3, we see that the performance of IMLE is very close to that of IMSE, and slightly superior at high SNR; we conjecture that IMLE is slightly more robust to the Gaussian-interference approximation. The PLIC trace in Fig. 3 bounds IMLE/IMSE performance through perfect *local* interference cancellation. Specifically, PLIC calculates LVs assuming that the ICI component of $\boldsymbol{s}_k^{(i)}$ in (22) is perfectly known, and treating the ISI/ICI components of $\boldsymbol{\epsilon}_k^{(i)}$ as noise. The proximity of PLIC to ML8 and MS8 (i.e., < 1 dB) shows that the turbo equalization algorithms are performing near-optimal ICI cancellation after eight iterations. The PGIC trace shows the performance of perfect *global* interference cancellation, i.e., perfect knowledge of all ISI/ICI when calculating LVs. The relatively small gap between PLIC and PGIC (i.e., < 1 dB) shows that the max-SINR pulses are performing near-optimal out-of-target ISI/ICI suppression. Fig. 3 shows that TOMS outperforms JOMS, which outperforms ROMS. We conjecture that the turbo-equalization algorithms benefit from the uncorrelated noise samples provided by TOMS. Between JOMS and ROMS,

[1]By "triple-Doppler," we refer to the case where the mobile is moving away from (towards) the base station with speed v and a strong reflector is moving towards (away from) *both* the base station and the mobile with speed v, so that the reflected path length changes at a rate of $\pm 3v$, producing a single-sided Doppler spread of $f_{\text{d}}T_c = 3vf_c c^{-1}$, where c denotes the speed of light [26]. Such a "triple Doppler" case can occur, e.g., when the base station is located close to a highway on which the mobile and scatterer are driving in opposite directions.

[2]The interleaver reads a sequence of $N_i MN$ coded-bits column-wise into an $N_i \times MN$ array. The rows of the array are then shuffled such that the kth row forms the $(\lfloor (k/N_p) \rfloor + (N_i/N_p)\langle k \rangle_{N_p})$th row of the shuffled array, where N_p is a suitably chosen divisor of N_i. Finally, bits are read row-wise from the shuffled array. For our experiments, we chose $N_i = 40$ and $N_p = 10$. Note that, in this case, the first three coded-bits are distributed to MC-symbols with indices 0, 4, and 8, respectively, within the 40-MC-symbol block. With a coherence time of $(f_{\text{d}}T_c N)^{-1} \approx 5$ MC-symbols, this interleaving scheme ensures that any $N_p = 10$ adjacent coded-bits will experience reasonably uncorrelated fading.

[3]We assume that 40-MC-symbol decoding delays are tolerable. Smaller N_i would reduce the decoding delay but increase the probability that an entire code-block experiences a deep fade.

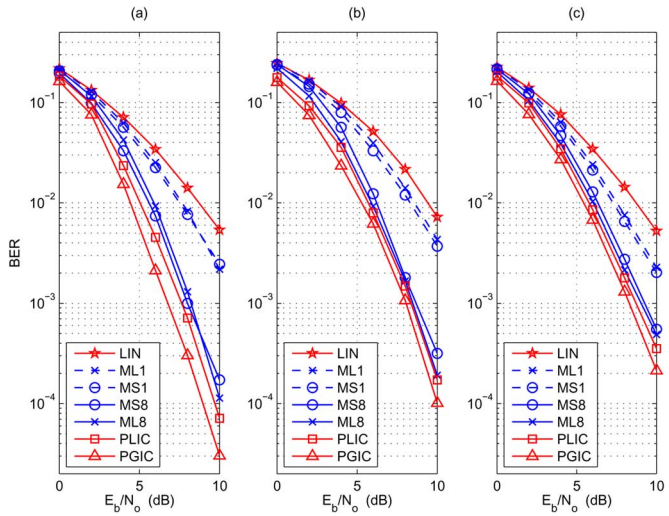

Fig. 3. Coded BER performance of QAM-MCM with (a) TOMS, (b) JOMS, and (c) ROMS pulses under various equalization/decoding strategies.

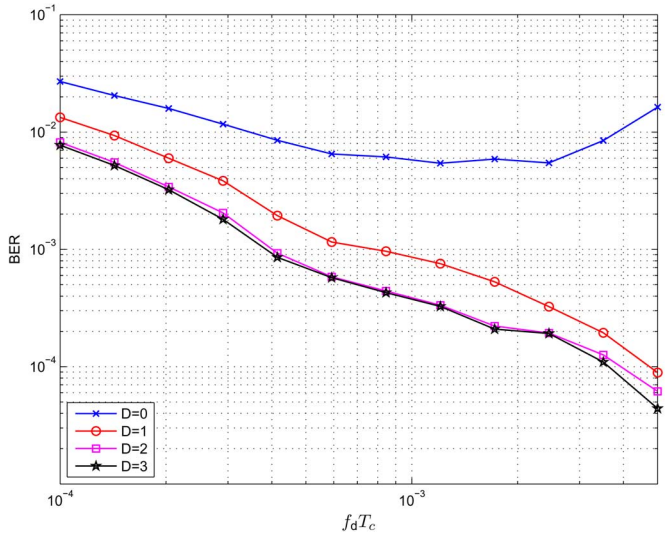

Fig. 4. Coded BER performance of TOMS-QAM-MCM versus f_dT_c at SNR $= 10$ dB using 8-iteration IMLE and various choices of ICI radius D.

which both induce noise correlation, JOMS better suppresses ISI/ICI. For reference, LIN shows the performance of (non-iterative) linear MMSE equalization followed by decoding. Note that the MAP-based iterative equalizers significantly outperform the linear MMSE scheme.

Fig. 4 shows BER versus f_dT_c (at SNR $= 10$ dB) for TOMS-QAM-MCM with 8-iteration IMLE using various choices of ICI radius D. Though it can be seen that performance improves uniformly with D, the choice $D = 2$ performs nearly as well as $D = 3$ over the f_dT_c range considered. Since complexity is proportional to D^3 (or D^2, depending on IMLE's matrix inversion algorithm), we favor the complexity/performance tradeoff offered by $D = 2$. Notice that, with adequate D (here, $D \geq 1$), performance improves with f_dT_c as a consequence of Doppler diversity. With inadequate D (here, $D = 0$), losses due to out-of-target ISI/ICI dominate gains from Doppler diversity, and performance decreases with f_dT_c.

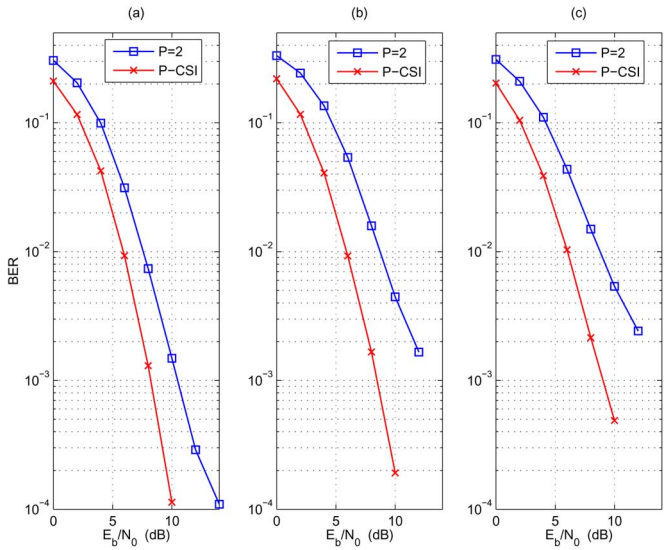

Fig. 5. Coded BER performance of QAM-MCM under 8-iteration IMLE using perfect CSI and pilot-aided ($P = 2$) Wiener channel estimates for (a) TOMS, (b) JOMS, and (c) ROMS pulses.

Fig. 5 repeats the 8-iteration IMLE experiments of Fig. 3 with imperfect channel estimates. For this, we used the reduced-rank pilot-aided Wiener estimation scheme from [30]. In particular, a pilot MC-symbol was inserted every P data MC-symbols, and pairs of consecutive pilot MC-symbols were used to estimate the channel coefficients of the $P - 1$ data MC-symbols in between. By channel coefficients, we mean the $(2D + 1)N$ significant coefficients of $\boldsymbol{H}^{(i,0)}$. (See [30] for more details.) In Fig. 5, we see that, when $P = 2$, the use of imperfect channel estimates induces an SNR loss of approximately 2–3 dB. While the resulting modulation efficiency of $\eta = 0.5$ complex- symbols/s/Hz may not not seem very high, it equals that of the typical BO-QAM-MCM scheme (e.g., [2], [3], [6]) *before* pilots are added.

B. Performance Relative to Other QAM-MCM Schemes

To compare our max-SINR schemes to BO-QAM-MCM, we simulated coded versions of standard CP-OFDM [19], as well as Strohmer/Beaver's orthogonal [6, eq. (18)], and biorthogonal [6, eq. (61)], QAM-MCM, and equalized with IMLE using ICI radius $D = 2$ and eight turbo iterations. For Strohmer/Beaver (bi)orthogonal QAM-MCM, we numerically optimized the pulses to minimize the total ISI-plus-ICI power, assuming a rectangular time–frequency lattice (as before). For fair comparison with the proposed max-SINR QAM-MCM schemes, we used modulation efficiency $\eta = 0.744$ QPSK-symbols/s/Hz (as recommended by [6], Fig. 1,) in conjunction with the 1.25dB-gain rate-2/3 convolutional code from [28, Table 11.d], yielding a rate of 0.992 information-bits/s/Hz. For CP-OFDM, we assumed the ISI-suppressing guard interval $N_g = N_h - 1$, yielding modulation efficiency $\eta = 0.81$ QPSK-symbols/s/Hz, and the same 1.25 dB-gain rate-2/3 convolutional code from [28, Table 11.d], yielding 1.08 information-bits/s/Hz. Fig. 6 shows that the Strohmer/Beaver orthogonal and biorthogonal schemes, denoted by S-OFDM and S-BDFM, respectively, suffer from SNR losses of about 1 dB from the best max-SINR schemes (i.e., TOMS and

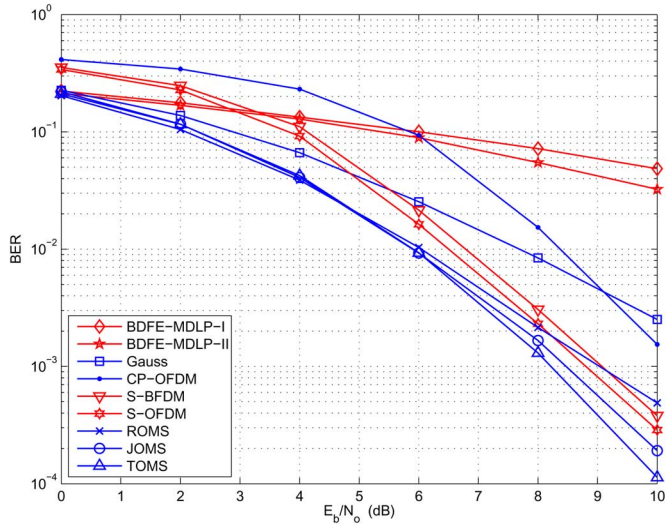

Fig. 6. Coded BER performance of MDLP-BDFE (lowest complexity and best performing designs) and of 8-iteration IMLE on various QAM-MCM schemes: Strohmer's OFDM, Strohmer's BDFM, ROMS, TOMS, JOMS, and ISI/ICI-suppressing Gaussian pulses.

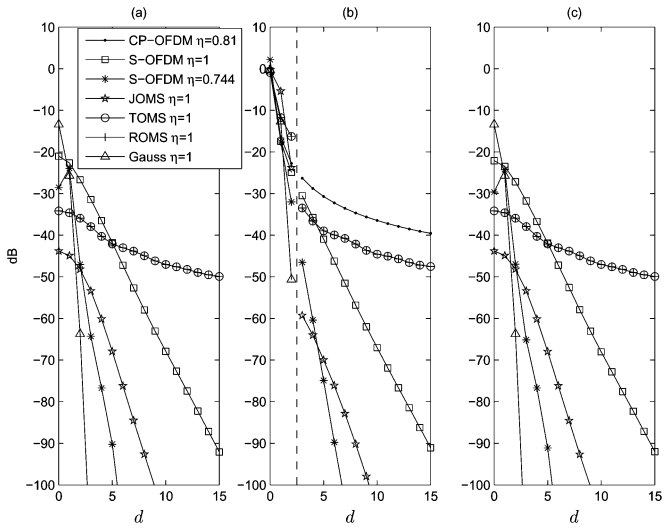

Fig. 7. ISI/ICI profiles for various QAM-MCM schemes at SNR $= 8$ dB. In particular, $E\{|H^{(\cdot,\ell)}(d,\cdot)|^2\}$ is shown versus d for (a) $\ell = -1$, (b) $\ell = 0$, and (c) $\ell = 1$.

JOMS), even though the code used with the Strohmer/Beaver schemes had a higher coding gain. We conjecture that this performance loss results from BO-QAM-MCM's higher levels of out-of-target ISI/ICI. Recall that BO-QAM-MCM attempts to suppress *all* ISI/ICI, a goal that is perhaps too difficult to achieve, while our max-SINR QAM-MCM attempts to suppress only *out-of-target* ISI/ICI, an achievable goal. Fig. 6 shows that CP-OFDM suffers an SNR loss of about 2.5 dB from the best max-SINR scheme, which can be attributed to CP-OFDM's relatively high levels of out-of-target ICI.

To compare against traditional ISI/ICI *suppressing* as opposed to ISI/ICI *shaping* NBO-QAM-MCM schemes (e.g., [12], [31]), we investigated the use of Gaussian pulses which minimize total ICI-plus-ISI power. The remaining modulation, coding, equalization, and decoding parameters were chosen as before, including the use of IMLE with ICI radius $D = \lceil f_d T_c N + 1 \rceil = 2$. From Fig. 6, we see that the BER performance of this ISI/ICI-suppressing scheme lags behind that of the ISI/ICI-shaping schemes, especially at high SNR, as a result of nonnegligible out-of-target ISI/ICI.

The perf'ormance of a particular QAM-MCM scheme can be inferred in part from its ISI/ICI profile, i.e., $E\{|H^{(i,\ell)}(d,k)|^2\}$ for $d \in \{0,\ldots,N-1\}$ and $\ell \in \{-L_{\text{pre}},\ldots,L_{\text{pst}}\}$. [Recall from (10) that there is no dependence on i and k.] Since the coefficients $\{H^{(\cdot,0)}(d,\cdot)\}_{d=-D}^{D}$ are used in symbol detection, it is generally good for them to be large; since all other coefficients generate out-of-target ISI and ICI, it is generally good for them to be small. Fig. 7 shows $E\{|H^{(\cdot,\ell)}(d,\cdot)|^2\}$ for several pulse designs at SNR $= 8$ dB. In particular, Fig. 7(a) shows pre-cursor ISI, Fig. 7(c) shows post-cursor ISI, and Fig. 7(b) shows out-of-target ICI to the right of the dashed line and in-target ICI to the left. From Fig. 7, we see that JOMS does an excellent job of maintaining in-target energy while suppressing out-of-target energy, even at the high modulation efficiency of $\eta = 1$ complex-symbol/s/Hz. Both TOMS and ROMS (which have identical ISI/ICI profiles), also maintain high in-target energy and reasonably low

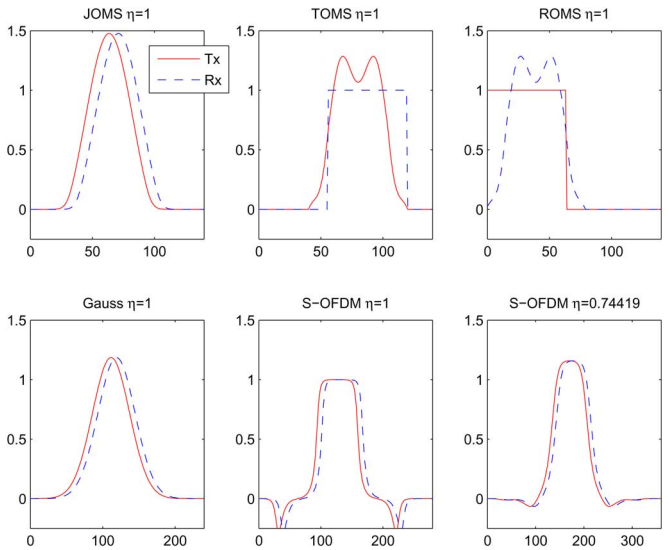

Fig. 8. Pulse shapes for various QAM-MCM schemes at SNR $= 8$ dB.

out-of-target energy at $\eta = 1$. S-OFDM also does a good job of ISI/ICI suppression at $\eta = 0.744$, though ISI suppression suffers at $\eta = 1$. CP-OFDM with guard $N_g = N_h - 1$ (and, hence, $\eta = 0.81$) perfectly suppresses ISI, but does a poor job of suppressing out-of-target ICI. Gaussian pulses which attempt to suppress all ISI/ICI have difficulty in doing so when $\eta = 1$, motivating the ISI/ICI-shaping techniques considered here.

The modulation and demodulation pulses of the various QAM-MCM schemes are plotted in Fig. 8 for the setup described above at SNR $= 8$ dB. There, it can be seen that the JOMS pulse looks much narrower than the ISI/ICI-suppressing Gaussian pulse and a bit more "triangular," while the TOMS, ROMS, and S-OFDM $\eta = 1$ pulses look very non-Gaussian. It can also be seen that the TOMS pulses are duals of the ROMS pulses.

C. Performance and Complexity Relative to MDLP

Next we compare against the maximum diversity linear precoding (MDLP) scheme of Ma and Giannakis [16]. MDLP assumes that, over a block duration of RN, the channel is well modeled by a basis expansion of order $Q = \lceil 2f_{\mathsf{d}}T_cRN \rceil$. It then partitions the RN-length block into R MC-symbols of N subcarriers each, incorporating length-$(N_h - 1)$ time-domain guards and length-Q frequency-domain guards, for an overall modulation efficiency of $\eta = (N - Q)(R - N_h + 1)/(RN)$ complex-symbols/s/Hz. For the channel parameters $f_{\mathsf{d}}T_c = 0.003$ and $N_h = 16$, and for any choice of $[R, N]$, it can be shown that MDLP efficiency is limited to $\eta_{\max} = 0.49$ complex-symbols/s/Hz. Though several combinations of $[R, N]$ are capable of yielding $\eta \approx \eta_{\max}$, all of them yield $RN > 100$, for which optimal decoding becomes impractical.[4] For this reason, we focused on suboptimal MDLP reception via block decision feedback equalization (BDFE) [17]. Though we tested MDLP-BDFE exhaustively for all $[R, N]$ which gave modulation efficiencies between 0.48 and $\eta_{\max}$, we focus here on the best-performance and least-complexity designs: $[R, N] = [52, 16]$ and $[R, N] = [55, 3]$, respectively.[5] With QPSK, both designs yielded spectral efficiencies of about 0.98 information-bits/s/Hz, which allows a fair comparison to the coded QAM-MCM schemes.

Fig. 6 shows that MDLP-BDFE does not perform as well as the coded QAM-MCM schemes over the SNR range of interest. To understand why, recall that high diversity does not guarantee good BER performance at moderate to low SNRs, and that BDFE detection may not fully exploit the available diversity. In addition, MDLP's low modulation efficiency does not leave room for finite-field coding, which could have boosted low-SNR performance through coding gain.

We now compare the complexity of MDLP with BDFE [17] to that of QAM-MCM with IMLE/IMSE. Complexity will be quantified in complex floating point operations (cflops) per channel use (pcu). Using fast Fourier transforms (FFTs), the cost of demodulation for both MDLP and QAM-MCM is identical and approximately $1 + (3/2)\log_2 N$ cflops pcu. IMLE consumes approximately $39D^3 + 88D^2 + 56D + 22$ cflops pcu, while IMSE consumes approximately $102D^3 + 280D^2 + 222D + 66$ cflops pcu [34]. For QAM-MCM, we can ignore the complexity of convolutional decoding, since it is small relative to that of iterative equalization. Though we also derived expressions for MDLP-BDFE complexity in terms of $[R, N, L_e, Q_e, L_b, Q_b]$ (see [34]), they are somewhat lengthy and, as a consequence, not presented here.

Fig. 9 shows the ratio of MDLP-BDFE complexity to QAM-MCM-IMLE complexity over a range of delay and Doppler spreads.[6] There, the solid lines are complexity-ratio contours,

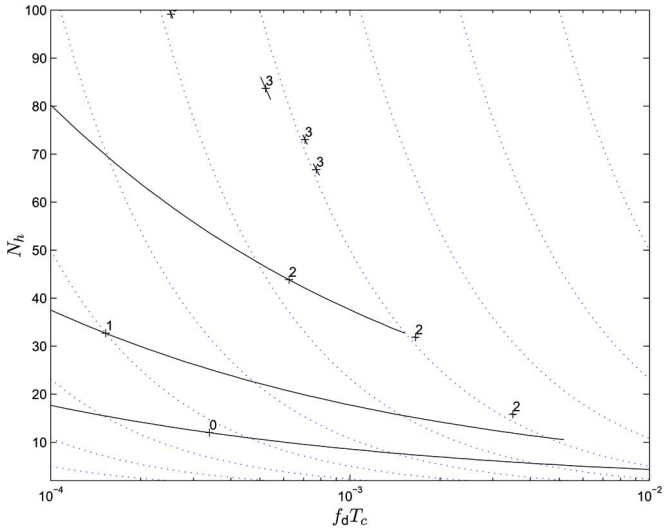

Fig. 9. Solid lines are contours of the MDLP-BDFE versus QAM-MCM-IMLE complexity ratio, where contour label ρ indicates that MDLP-BDFE is 10^{ρ} times as complex as QAM-MCM-IMLE. Dotted lines are iso-spreading-factor contours. There were no admissible MDLP-BDFE designs for spreading factors $\zeta > 0.1$.

where contour height "ρ" indicates that BDFE is 10^{ρ} times as complex as IMLE. Thus, the region above the "0"-labeled contour corresponds to delay/Doppler spreads where IMLE is cheaper than BDFE. From Fig. 9, it is clear that IMLE is cheaper[7] for all but very small delay spreads—and several orders-of-magnitude cheaper at large delay spreads, which is noteworthy considering that QAM-MCM-IMLE significantly outperforms MDLP-BDFE. In Fig. 9, we found it convenient to superimpose iso-spreading-factor contours as dotted lines, where the spreading factor $\zeta := 2f_{\mathsf{d}}T_cN_h$—the product of delay and Doppler spreads—quantifies the overall channel severity.

VI. Conclusion

In this paper, we presented a new approach to coded QAM-MCM for doubly dispersive channels. Non-(bi)orthogonal pulses were designed to *shape* the ISI/ICI into a pattern that enables simple yet high-performance equalization, for which two turbo equalizers were presented. Numerical results demonstrated that the proposed max-SINR QAM-MCM system yields coded BER performance that surpasses (bi)orthogonal and non-(bi)orthogonal QAM-MCM systems based on total ISI/ICI suppression (rather than ISI/ICI shaping) as well as MDLP systems which use BDFE reception. For example, when employing turbo-equalization to extract the information contained in the dominant ISI/ICI, and for the "typical" channel parameters $f_{\mathsf{d}}T_c = 0.003$ and $N_h = 16$, we found that the proposed max-SINR pulses yield an SNR-gain of ≈ 1 dB over Strohmer/Beaver's optimal ISI/ICI-suppressing pulses [6] and ≈ 2.5 dB over standard CP-OFDM pulses. Comparing the proposed QAM-MCM scheme to MDLP-BDFE at 1 bit/s/Hz over the same channel, we found that the proposed scheme yielded simultaneous improvements in BER performance and implementation complexity (e.g., >6 dB SNR-gain and

[4]Consider that sphere decoding [32] significantly reduces ML decoding complexity only at high SNR [33], which, recalling Fig. 6, is not within our target operating range.

[5]The complete parameter settings, in the notation of [17], were $[Q, L_e, Q_e, L_b, Q_b, dL, db, dQ] = [5, 35, 15, 15, 7, 9, 3, 2]$ and $[Q, L_e, Q_e, L_b, Q_b, dL, db, dQ] = [1, 35, 14, 15, 4, 9, 3, 4]$, respectively.

[6]In generating Fig. 9, we assumed a QAM-MCM system with $N = 4N_h$, $N_s = N$, $D = \lceil f_{\mathsf{d}}T_cN + 1 \rceil$, and eight iterations. Likewise, we assumed a MDLP-BDFE system with $[L_e, Q_e, L_b, Q_b] = [2(N_h - 1), 2Q, N_h - 1, Q]$, $Q = \lceil 2f_{\mathsf{d}}T_cRN \rceil$ (to ensure reasonable performance), and $[R, N]$ set to minimize complexity subject to $\eta \geq 0.45$ complex-symbols/s/Hz. Note: there did not exist any $[R, N]$ yielding $\eta \geq 0.45$ for spreading factor $\zeta > 0.1$.

[7]As an example, QAM-MCM-IMLE is about 1/20th the complexity of MDLP-BDFE when $f_{\mathsf{d}}T_c = 0.003$ and $N_h = 16$, i.e., the channel parameters assumed throughout most of this section.

factor-of-20 complexity reduction, respectively). As possible future work, one might consider extending the proposed scheme to MCM systems using offset-QAM [5] or nonrectangular time–frequency lattices [6].

APPENDIX A
DERIVATION OF (35)

First, we expand $p(\boldsymbol{y}_k|s_k=\psi(\boldsymbol{\gamma}))$ using (29)

$$p(\boldsymbol{y}_k|s_k=\psi(\boldsymbol{\gamma})) = C\exp\Big[-\frac{1}{2}(\boldsymbol{y}_k-\psi(\boldsymbol{\gamma})\boldsymbol{h}_{k,0})^H \times \boldsymbol{\Sigma}_{\boldsymbol{q}_k}^{-1}(\boldsymbol{y}_k-\psi(\boldsymbol{\gamma})\boldsymbol{h}_{k,0})\Big] \quad (48)$$

$$= C\exp\Big[-\frac{1}{2}\boldsymbol{y}_k^H\boldsymbol{\Sigma}_{\boldsymbol{q}_k}^{-1}\boldsymbol{y}_k - \frac{1}{2}|\psi(\boldsymbol{\gamma})|^2\boldsymbol{h}_{k,0}^H\boldsymbol{\Sigma}_{\boldsymbol{q}_k}^{-1}\boldsymbol{h}_{k,0}\Big] \cdot \exp\left[\mathrm{Re}\ (\psi(\boldsymbol{\gamma})g_k)\right]. \quad (49)$$

Since the first exponential in (49) is invariant to $\boldsymbol{\gamma}$ (recalling the PSK assumption), its contributions to the numerator and denominator of (34) cancel. From $(P(c_{k,m}=0)/P(c_{k,m}=1)) = e^{L_{\mathrm{old}}(k,m)}$, we find

$$P(c_{k,m'}=0) = \frac{e^{L_{\mathrm{old}}(k,m')}}{e^{L_{\mathrm{old}}(k,m')}+1} \quad (50)$$

$$= \frac{e^{L_{\mathrm{old}}(k,m')/2}}{2\cosh\left(\frac{L_{\mathrm{old}}(k,m')}{2}\right)} \quad (51)$$

$$P(c_{k,m'}=1) = \frac{e^{-L_{\mathrm{old}}(k,m')/2}}{2\cosh\left(\frac{L_{\mathrm{old}}(k,m')}{2}\right)}. \quad (52)$$

Together

$$P(c_{k,m'}=\gamma_{m'}) = \frac{\exp\left[(-1)^{\gamma_{m'}}\frac{L_{\mathrm{old}}(k,m')}{2}\right]}{2\cosh\left(\frac{L_{\mathrm{old}}(k,m')}{2}\right)}. \quad (53)$$

Since $\cosh(L_{\mathrm{old}}(k,m')/2)$ is invariant to $\gamma_{m'}$, its contributions to the numerator and denominator of (34) cancel. The remaining terms yield (35).

APPENDIX B
UPDATE OF MEAN, VARIANCE, AND LV

The quantities μ_k and v_k can be updated using $\{L_{\mathrm{old}}(k,m)\}_{m=0}^{M-1}$ as follows. First, we rewrite (25) as

$$\mu_k = \sum_{\boldsymbol{\gamma}\in\{0,1\}^M}\psi(\boldsymbol{\gamma})\prod_{m=0}^{M-1}P(c_{k,m}=\gamma_m).$$

using the bit independence assumption introduced in Section IV-B. For QPSK (i.e., $M=2$) we have

$$\psi(\boldsymbol{\gamma}) = \frac{1}{\sqrt{2}}\left[(-1)^{\gamma_0}+j(-1)^{\gamma_1}\right] \quad (54)$$

so that

$$\mu_k = \frac{1}{\sqrt{2}}\sum_{\gamma_0=0}^{1}(-1)^{\gamma_0}P(c_{k,0}=\gamma_0)\sum_{\gamma_1=0}^{1}P(c_{k,1}=\gamma_1) + \frac{j}{\sqrt{2}}\sum_{\gamma_1=0}^{1}(-1)^{\gamma_1}P(c_{k,1}=\gamma_1)\sum_{\gamma_0=0}^{1}P(c_{k,0}=\gamma_0) \quad (55)$$

$$= \frac{1}{\sqrt{2}}\tanh\left(\frac{L_{\mathrm{old}}(k,0)}{2}\right)+\frac{j}{\sqrt{2}}\tanh\left(\frac{L_{\mathrm{old}}(k,1)}{2}\right). \quad (56)$$

To calculate v_k, we note, from (26) in the QPSK case, that $|\beta|=1\,\forall\,\beta\in\mathbb{S}$, so that $v_k=1-|\mu_k|^2$. Similarly, it can be seen that $v_{k,R}=1/2-(\mathrm{Re}\,\mu_k)^2$ and $v_{k,I}=1/2-(\mathrm{Im}\,\mu_k)^2$. Notice that, with uncorrelated real and imaginary symbol components, $v_k=v_{k,R}+v_{k,I}$.

The LV update reduces to the calculation of $\Delta L_{\mathrm{IMLE}}(k,m)$ and $\Delta L_{\mathrm{IMSE}}(k,m)$ for the IMLE and IMSE algorithms, respectively. For QPSK (i.e., $M=2$), the IMLE quantities are as shown in (57) and (58) at the bottom of the page, where (58) was derived in a manner similar to (57) [35]. To derive the IMSE

$$\Delta L_{\mathrm{IMLE}}(k,0) = \ln\frac{\sum_{\gamma_1=0}^{1}\exp\left[\mathrm{Re}\,(\psi([0,\gamma_1])g_k)+\frac{1}{2}(-1)^{\gamma_1}L_{\mathrm{old}}(k,1)\right]}{\sum_{\gamma_1=0}^{1}\exp\left[\mathrm{Re}\,(\psi([1,\gamma_1])g_k)+\frac{1}{2}(-1)^{\gamma_1}L_{\mathrm{old}}(k,1)\right]}$$

$$= \ln\frac{\exp[\frac{1}{\sqrt{2}}\mathrm{Re}\,g_k]\sum_{\gamma_1=0}^{1}\exp\left[-\frac{1}{\sqrt{2}}\mathrm{Im}\,((-1)^{\gamma_1}g_k)+\frac{1}{2}(-1)^{\gamma_1}L_{\mathrm{old}}(k,1)\right]}{\exp[-\frac{1}{\sqrt{2}}\mathrm{Re}\,g_k]\sum_{\gamma_1=0}^{1}\exp\left[-\frac{1}{\sqrt{2}}\mathrm{Im}\,((-1)^{\gamma_1}g_k)+\frac{1}{2}(-1)^{\gamma_1}L_{\mathrm{old}}(k,1)\right]}$$

$$= \sqrt{2}\mathrm{Re}\,g_k \quad (57)$$

$$\Delta L_{\mathrm{IMLE}}(k,1) = -\sqrt{2}\mathrm{Im}\,g_k \quad (58)$$

$$\Delta L_{\mathrm{IMSE}}(k,0)=\ln\frac{\sum_{\gamma_1=0}^{1}\exp\left[-\frac{\mathrm{Re}^2(\hat{s}_k-\bar{s}_{k,[0,\gamma_1]})}{2\sigma_{k,R}^2}-\frac{\mathrm{Im}^2(\hat{s}_k-\bar{s}_{k,[0,\gamma_1]})}{2\sigma_{k,I}^2}+\frac{1}{2}(-1)^{\gamma_1}L_{\mathrm{old}}(k,1)\right]}{\sum_{\gamma_1=0}^{1}\exp\left[-\frac{\mathrm{Re}^2(\hat{s}_k-\bar{s}_{k,[1,\gamma_1]})}{2\sigma_{k,R}^2}-\frac{\mathrm{Im}^2(\hat{s}_k-\bar{s}_{k,[1,\gamma_1]})}{2\sigma_{k,I}^2}+\frac{1}{2}(-1)^{\gamma_1}L_{\mathrm{old}}(k,1)\right]} \tag{59}$$

quantities, we start with (59), shown at the top of the page. We use $\bar{s}_{k,[\gamma_0,\gamma_1]}=\psi([\gamma_0,\gamma_1])\boldsymbol{f}_k^H\boldsymbol{h}_{k,0}$ to form

$$\begin{aligned}\mathrm{Re}^2(\hat{s}_k-\bar{s}_{k,[0,\gamma_1]})&=\mathrm{Re}^2(\hat{s}_k)-\sqrt{2}\mathrm{Re}\,(\hat{s}_k)\boldsymbol{f}_k^H\boldsymbol{h}_{k,0}+\frac{1}{2}(\boldsymbol{f}_k^H\boldsymbol{h}_{k,0})^2\\ \mathrm{Re}^2(\hat{s}_k-\bar{s}_{k,[1,\gamma_1]})&=\mathrm{Re}^2(\hat{s}_k)+\sqrt{2}\mathrm{Re}\,(\hat{s}_k)\boldsymbol{f}_k^H\boldsymbol{h}_{k,0}+\frac{1}{2}(\boldsymbol{f}_k^H\boldsymbol{h}_{k,0})^2.\end{aligned}$$

Since $\mathrm{Im}^2(\hat{s}_k-\bar{s}_{k,[0,\gamma_1]})=\mathrm{Im}^2(\hat{s}_k-\bar{s}_{k,[1,\gamma_1]})$, we pull the $\exp[\sqrt{2}/(2\sigma_{k,R}^2)\mathrm{Re}\,(\hat{s}_k)\boldsymbol{f}_k^H\boldsymbol{h}_{k,0}]$ terms out from the γ_1-summations, cancel common terms, and find

$$\Delta L_{\mathrm{IMSE}}(k,0)=\frac{\sqrt{2}\mathrm{Re}\,(\hat{s}_k)\boldsymbol{f}_k^H\boldsymbol{h}_{k,0}}{\sigma_{k,R}^2}.$$

A similar derivation yields [35]

$$\Delta L_{\mathrm{IMSE}}(k,1)=\frac{\sqrt{2}\mathrm{Im}\,(\hat{s}_k)\boldsymbol{f}_k^H\boldsymbol{h}_{k,0}}{\sigma_{k,I}^2}.$$

Appendix C
Derivation of (42) and (43)

Say $\bar{\boldsymbol{x}}_k:=\boldsymbol{x}_k-\boldsymbol{H}_k\boldsymbol{\mu}_k$ so that $\hat{s}_k=\boldsymbol{f}_k^H\bar{\boldsymbol{x}}_k$. The real part of $\hat{s}_k$ can be expressed as

$$\mathrm{Re}\,(\hat{s}_k)=\frac{1}{2}\begin{bmatrix}\boldsymbol{f}_k\\ \boldsymbol{f}_k^*\end{bmatrix}^H\begin{bmatrix}\bar{\boldsymbol{x}}_k\\ \bar{\boldsymbol{x}}_k^*\end{bmatrix}. \tag{60}$$

Then it follows that

$$\begin{aligned}\sigma_{k,R}^2&=\frac{1}{4}\begin{bmatrix}\boldsymbol{f}_k\\ \boldsymbol{f}_k^*\end{bmatrix}^H\mathrm{Cov}\left(\begin{bmatrix}\bar{\boldsymbol{x}}_k\\ \bar{\boldsymbol{x}}_k^*\end{bmatrix}\middle| s_k=\psi(\boldsymbol{\gamma})\right)\begin{bmatrix}\boldsymbol{f}_k\\ \boldsymbol{f}_k^*\end{bmatrix}\\ &=\frac{1}{4}\begin{bmatrix}\boldsymbol{f}_k\\ \boldsymbol{f}_k^*\end{bmatrix}^H\begin{bmatrix}\boldsymbol{\Sigma}_{\bar{\boldsymbol{x}}_k|s_k}&\tilde{\boldsymbol{\Sigma}}_{\bar{\boldsymbol{x}}_k|s_k}\\ \tilde{\boldsymbol{\Sigma}}_{\bar{\boldsymbol{x}}_k|s_k}^*&\boldsymbol{\Sigma}_{\bar{\boldsymbol{x}}_k|s_k}\end{bmatrix}\begin{bmatrix}\boldsymbol{f}_k\\ \boldsymbol{f}_k^*\end{bmatrix}\end{aligned}$$

where, assuming CWGN and symbols with uncorrelated real and imaginary components

$$\begin{aligned}\boldsymbol{\Sigma}_{\bar{\boldsymbol{x}}_k|s_k}&=\boldsymbol{H}_k\mathcal{D}(\boldsymbol{v}_k)\boldsymbol{H}_k^H+\boldsymbol{\Sigma}_{\boldsymbol{\varepsilon}_k}\\ \tilde{\boldsymbol{\Sigma}}_{\bar{\boldsymbol{x}}_k|s_k}&:=E\big\{(\bar{\boldsymbol{x}}_k-E\{\bar{\boldsymbol{x}}_k|s_k=\psi(\boldsymbol{\gamma})\})\\ &\qquad\times(\bar{\boldsymbol{x}}_k-E\{\bar{\boldsymbol{x}}_k|s_k=\psi(\boldsymbol{\gamma})\})^t\,\big|s_k=\psi(\boldsymbol{\gamma})\big\}\\ &=\boldsymbol{H}_k\mathcal{D}(\boldsymbol{v}_{k,R}-\boldsymbol{v}_{k,I})\boldsymbol{H}_k^t\end{aligned}$$

for $\boldsymbol{v}_k$ from (33), $\boldsymbol{v}_{k,R}$ from (44), and $\boldsymbol{v}_{k,I}$ from (45). Putting the above equations together gives (42). Using

$$\mathrm{Im}\,(\hat{s}_k)=\frac{1}{2}\begin{bmatrix}\boldsymbol{f}_k\\ -\boldsymbol{f}_k^*\end{bmatrix}^H\begin{bmatrix}\bar{\boldsymbol{x}}_k\\ \bar{\boldsymbol{x}}_k^*\end{bmatrix}$$

and similar methods, we arrive at (43).

Appendix D
Derivation of (47)

Using the conditionally Gaussian assumption described in Section IV-D

$$p(\hat{s}_k|s_k=\psi(\boldsymbol{\gamma}))=C\cdot\exp\left[-\frac{\mathrm{Re}^2(\hat{s}_k-\bar{s}_k)}{2\sigma_{k,R}^2}-\frac{\mathrm{Im}^2(\hat{s}_k-\bar{s}_k)}{2\sigma_{k,I}^2}\right] \tag{61}$$

which accounts for the first two terms in the exponentials in (47). Next, recall that $P(c_{k,m'}=\gamma_{m'})$ can be written as in (53). Substituting (53) into (46), the $\cosh(L_{\mathrm{old}}(k,m')/2)$ contributions from numerator and denominator cancel (since they are invariant to $\gamma_{m'}$), and what remains accounts for the third term in the exponentials of (47).

References

[1] B. L. Floch, M. Alard, and C. Berrou, "Coded orthogonal frequency division multiplex," *Proc. IEEE*, vol. 83, no. 6, pp. 982–996, Jun. 1995.

[2] R. Haas and J.-C. Belfiore, "A time-frequency well-localized pulse for multiple carrier transmission," *Wireless Pers. Commun.*, vol. 5, pp. 1–18, Jul. 1997.

[3] W. Kozek and A. F. Molisch, "Nonorthogonal pulseshapes for multicarrier communications in doubly dispersive channels," *IEEE J. Sel. Areas Commun.*, vol. 16, no. 10, pp. 1579–1589, Oct. 1998.

[4] D. Schafhuber, G. Matz, and F. Hlawatsch, "Pulse-shaping OFDM/BFDM systems for time-varying channels: ISI/ICI analysis, optimal pulse design, and efficient implementation," in *Proc. IEEE Symp. PIMRC*, Sep. 2002, pp. 1012–1016.

[5] H. Bölcskei, "Orthogonal frequency division multiplexing based on offset QAM," in *Advances in Gabor Theory*, H. G. Feichtinger and T. Strohmer, Eds. Basel, Switzerland: Birkhäuser, 2002, pp. 321–352.

[6] T. Strohmer and S. Beaver, "Optimal OFDM design for time-frequency dispersive channels," *IEEE Trans. Commun*, vol. 51, no. 7, pp. 1111–1122, Jul. 2003.

[7] I. Daubechies, *Ten Lectures on Wavelets*. Philadelphia, PA: SIAM, 1992.

[8] R. Koetter, A. C. Singer, and M. Tüchler, "Turbo equalization," *IEEE Signal Process. Mag.*, vol. 21, no. 1, pp. 67–80, Jan. 2004.

[9] M. Tüchler, A. Singer, and R. Koetter, "Minimum mean square error equalization using a priori information," *IEEE Trans. Signal Process.*, vol. 50, no. 3, pp. 673–683, Mar. 2002.

[10] D. Pham, J. Luo, K. R. Pattipati, and P. K. Willett, "A PDA-Kalman approach to multiuser detection in asynchronous CDMA," *IEEE Commun. Lett.*, vol. 6, no. 11, pp. 475–477, Nov. 2002.

[11] S. Liu and Z. Tian, "Near-optimal soft decision equalization for frequency selective MIMO channels," *IEEE Trans. Signal Process.*, vol. 52, no. 3, pp. 721–733, Mar. 2004.

[12] K. Matheus and K.-D. Kammeyer, "Optimal design of a multicarrier system with soft impulse shaping including equalization in time or frequency direction," in *Proc. IEEE Global Telecommun. Conf.*, 1997, vol. 1, pp. 310–314.
[13] K. Matheus, K. Knoche, M. Feuersänger, and K.-D. Kammeyer, "Two-dimensional (recursive) channel equalization for multicarrier systems with soft impulse shaping (MCSIS)," in *Proc. IEEE Global Telecommun. Conf.*, 1998, vol. 2, pp. 956–961.
[14] T. Hunziker and D. Dahlhaus, "Iterative detection for multicarrier transmission employing time-frequency concentrated pulses," *IEEE Trans. Commun.*, vol. 51, no. 4, pp. 641–651, Apr. 2003.
[15] P. Schniter, "Low-complexity equalization of OFDM in doubly selective channels," *IEEE Trans. Signal Process.*, vol. 52, no. 4, pp. 1002–1011, Apr. 2004.
[16] X. Ma and G. B. Giannakis, "Maximum-diversity transmissions over doubly selective wireless channels," *IEEE Trans. Inf. Theory*, vol. 49, no. 7, pp. 1832–1840, Jul. 2003.
[17] Z. Tang and G. Leus, "A receiver architecture for maximum diversity transmissions over doubly selective channels," in *Proc. IEEE Workshop Signal Process. Adv. Wireless Commun.*, 2005, pp. 171–175.
[18] J. G. Proakis, *Digital Communications*, 4th ed. New York: McGraw-Hill, 2001.
[19] L. J. Cimini, Jr, "Analysis and simulation of a digital mobile radio channel using orthogonal frequency division multiplexing," *IEEE Trans. Commun.*, vol. 33, no. 6, pp. 665–765, Jul. 1985.
[20] P. Schniter, "On the design of non-(bi)orthogonal pulse-shaped FDM for doubly dispersive channels," in *Proc. IEEE Int. Conf. Acoust., Speech, Signal Process.*, 2004, pp. iii-817–820.
[21] C. Douillard, M. Jezequel, C. Berrou, A. Picart, P. Didier, and A. Glavieux, "Iterative correction of intersymbol interference: Turbo equalization," *Eur. Trans. Telecommun.*, vol. 6, pp. 507–511, Sep.–Oct. 1995.
[22] X. Cai and G. B. Giannakis, "Bounding performance and suppressing inter-carrier interference in wireless mobile OFDM," *IEEE Trans. Commun.*, vol. 51, no. 12, pp. 2047–2056, Dec. 2003.
[23] L. Rugini, P. Banelli, and G. Leus, "Simple equalization of time-varying channels for OFDM," *IEEE Commun. Lett.*, vol. 9, no. 7, pp. 619–621, Jul. 2005.
[24] H. V. Poor, *An Introduction to Signal Detection and Estimation*, 2nd ed. New York: Springer, 1994.
[25] W. C. Jakes, *Microwave Mobile Communications*. New York: Wiley/IEEE Press, 1974.
[26] T. A. Thomas, T. P. Krauss, and F. W. Vook, "CHAMPS: A near-ML joint Doppler frequency/TOA search for channel characterization," in *Proc. IEEE Veh. Tech. Conf.*, Fall, 2003, pp. 74–78.
[27] D. B. Kilfoyle and A. B. Baggeroer, "The state of the art in underwater acoustic telemetry," *IEEE J. Ocean. Eng.*, vol. 25, no. 1, pp. 4–27, Jan. 2000.
[28] S. Lin and D. J. Costello, *Error Control Coding: Fundamentals and Applications*. Englewood Cliffs, NJ: Prentice-Hall, 1983.
[29] L. R. Bahl, J. Cocke, F. Jelinek, and J. Raviv, "Optimal decoding of linear codes for minimizing symbol error rate," *IEEE Trans. Inf. Theory*, vol. 20, no. 3, pp. 284–287, Mar. 1974.
[30] P. Schniter, "On doubly dispersive channel estimation for pilot-aided pulse-shaped multi-carrier modulation," in *Proc. 40th Annu. Conf. Inf. Sci. Syst.*, Mar. 2006, pp. 1296–1301.
[31] K. Liu, T. Kadous, and A. M. Sayeed, "Orthogonal time-frequency signaling over doubly dispersive channels," *IEEE Trans. Inf. Theory*, vol. 50, no. 11, pp. 2583–2603, Nov. 2004.
[32] E. Agrell, T. Eriksson, A. Vardy, and K. Zeger, "Closest point search in lattices," *IEEE Trans. Inf. Theory*, vol. 48, no. 8, pp. 2201–2214, Aug. 2002.
[33] J. Jalden and B. Ottersten, "On the complexity of sphere decoding in digital communications," *IEEE Trans. Signal Process.*, vol. 53, no. 4, pp. 1474–1484, Apr. 2005.
[34] S. Das, "Design and analysis of computationally efficient detection for multi-carrier modulation over multi-antenna doubly dispersive channels," Ph.D. dissertation, Ohio State Univ., Columbus, OH, Dec. 2007.
[35] S. Das, "Turbo equalization of pulse-shaped multi-carrier modulation in doubly dispersive channels," M.S. thesis, Ohio State Univ., Columbus, OH, Nov. 2004.

Sibasish Das received the B.Tech. degree in electronics and electrical communication engineering from the Indian Institute of Technology, Kharagpur, India, and the M.S. degree in electrical and computer engineering from The Ohio State University, Columbus, in 2002 and 2004, respectively. He is currently working towards the Ph.D. degree in electrical and computer engineering at The Ohio State University.

He was an intern with Texas Instruments, India, in 2001 and AMD Inc. in 2004. His current research interests include signal processing and communication theoretic aspects of time- and frequency-selective wireless channels, multiantenna and multicarrier communication.

Mr. Das was a recipient of the Jubilee Scholarship for Academic Excellence in 1998–2002 and The Ohio State University Fellowship in 2002–2003.

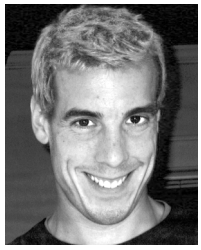

Philip Schniter received the B.S. and M.S. degrees in electrical and computer engineering from the University of Illinois at Urbana-Champaign in 1992 and 1993, respectively.

From 1993 to 1996, he was with Tektronix Inc., Beaverton, OR, as a Systems Engineer. In 2000, he received the Ph.D. degree in electrical engineering from Cornell University in Ithaca, NY. Subsequently, he joined the Department of Electrical and Computer Engineering at The Ohio State University, Columbus, OH, where he is now an Associate Professor. His research interests include signal processing, communication theory, and wireless networks.

Dr. Schniter received the National Science Foundation CAREER Award in 2003. Since 2005, he has served on the IEEE Signal Processing for Communications Technical Committee.